Compact high-power microwave oscillators

Philip MacInnes (Researcher)

Kevin Ronald (Co-Investigator)

Alan D. R. Phelps (Principal Investigator)

University of Strathclyde, Glasgow, Scotland, UK

GRANT: N62909-18-1-2122-GRANT12538355, N00014-18-S-B001

Final Report

Including SF298 Report Documentation Page

Period of Performance: 15 June 2018-14 June 2022

Report dated 30 September 2022

This work was sponsored by the Office of Naval Research (ONR), under grant (or contract) number N62909-18-1-2122, GRANT 12538355, N00014-18-S-B001. The views and conclusions contained herein are those of the authors only and should not be interpreted as representing those of ONR, the U.S. Navy, or the U.S. Government.

Grant or Contract Number: N62909-18-1-2122-GRANT12538355, N00014-18-S-B001
Date Prepared: 30 September 2022
Project Title: Compact high-power microwave oscillators
Final Report:
Principal Investigator: Alan Phelps, +44141 548 3166, a.d.r.phelps@strath.ac.uk
University of Strathclyde, Scotland, UK

Section I: Project Summary

1. Overview of Project

1.1 Abstract:

Numerical modeling and experimental measurements are reported of a novel high-power X-band ($8-12GHz$) microwave oscillator operating without the application of external magnetic insulation. Radiation is produced by modulation of an electron beam, propagated solely under the beam's self-forces. Numerical modeling indicates efficiencies of $\eta\sim25\%$, corresponding to $\sim220MW$ from a $500keV$, $1.7kA$ electron beam, with efficiencies of $\eta\sim30\%$ obtained as the quality of the electron beam improves through revision of the electron accelerator, informed by the experimental results. Named the 'Self-Insulating Backward-Wave Oscillator' (SIBWO), the prototype design has been manufactured for proof of principle experiments. The electron beam and the microwave output have been measured. The measured output mode TM_{01} and frequency of $9.25GHz$ both agree with the numerical model. The full-width-half-maximum microwave pulse duration $\sim50ns$ was shorter and the microwave power $\sim8MW$ was less than in the numerical simulations. Analysis of these results has identified modifications to enable increased output power in future work.

This work was sponsored by the Office of Naval Research (ONR), under grant (or contract) number N62909-18-1-2122, GRANT 12538355, N00014-18-S-B001. The views and conclusions contained herein are those of the authors only and should not be interpreted as representing those of ONR, the U.S. Navy, or the U.S. Government.

1.2 Objective:

Conventional High-Power Microwave (HPM) sources rely on the application of externally generated magnetic insulation to propagate their electron beams through a given interaction region. This adds to the complexity, weight, energy requirements and overall size of the source. The key objective of the presented work was to investigate the operation of an HPM source that mitigates those additional overheads, in weight etc., through the removal of the external magnet.

The source in question was nominally a novel variant of the relativistic Backward Wave Oscillator (BWO), building on earlier work performed at the University of Strathclyde (UoS) and separately at the Institute of High Current Electronics (IHCE), both focusing on operation in the S-band ($2 - 4GHz$). Termed the Self-Insulating Backward-Wave Oscillator (SIBWO), the source was designed to operate in the X-band ($8 - 12GHz$), nominally single frequency, with a target initial electronic efficiency of $\eta = 10\%$ and output powers of $\sim 100MW$.

The removal of the requirement for an external magnet means the electronic efficiency is significantly closer to the overall efficiency of the source, when compared with a conventional equivalent, making the SIBWO a much more practicable source for applications where weight, size and overall energy requirements are constrained. In addition, the relative simplicity of the source design lends itself to ruggedization in a manner that would not be possible with a conventional equivalent without adding significant additional complexity.

1.3 Introduction:

The University of Strathclyde (UoS) began work on the X-band Self-Insulating Backward-Wave Oscillator (SIBWO) in June 2018, with the project completing in June 2022 (including a no cost extension (NCE) due to the impact of the Covid-19 pandemic). The following report provides a technical overview of source operation, the predicted potential efficiency (via numerical simulations) and the first experimental results from a source prototype, including discussion of identified issues, potential solutions and considerations for future work.

Table 1: List of Acronyms and useful terms

ABP group	Atoms Beams and Plasmas research group, based in the Physics Department of the University of Strathclyde.
A-K gap	Anode – Cathode (German "Kathode") gap: the spacing between the cathodic emitter and anode plane of the electron accelerating diode
BWO	Backward-Wave Oscillator
CST	Computer Simulation Technology: Software used for electromagnetic and particle simulations. CST is owned by Dassault Systèmes.
EM	Electromagnetic (spectrum, pulse, field-pattern)
GHz	Giga-Hertz: 1,000,000,000 Hertz or 1,000,000,000 full-wave oscillations of the field-pattern per second.
HPM	High Power Microwave: typically $> 100MW$, though some scaling with frequency can apply.
IHCE	Institute of High Current Electronics, Tomsk, Russia
keV / kA	Kilo-electron-Volt / kilo-ampere: $1000\ Volts$ / $1000\ Amperes$
MW	Mega-Watt: $1{,}000{,}000\ Watts$
Ns	Nano-second: $0.000{,}000{,}001\ seconds$
NUDT	National University of Defense Technology, Hunan, China
PiC	Particle in Cell: a numerical code that considers both the electromagnetic fields and discrete particles within the "cells" used to define the simulation volume.
POF	Peak-Of-Field, maximum amplitude of EM field/ given EM field pattern
PPS	Pulsed Power Supply: a high voltage, high current single-shot power supply at the UoS, capable of producing ~250ns long pulses of up to 750kV (max as configured) at multiple tens of kiloamperes of current
S-band	A region of the EM spectrum between $2 - 4\ GHz$
SIBWO	Self-Insulating Backward-Wave Oscillator
SWS	Slow-wave structure
TE11	Transverse Electric 1,1 mode: The fundamental (simplest) supported field pattern in cylindrical waveguide.
TM01	Transverse Magnetic 0,1 mode: Intended operating mode of SIBWO.
UoS	University of Strathclyde, Glasgow, Scotland, United Kingdom
X-band	A region of the EM spectrum between $8 - 12GHz$
Hot / Cold measurement	'Hot' measurement: experiment with electron beam on 'Cold' measurement: measurement with electron beam off

Table 2: List of figures

1.4 Background and Supporting Theory.

The SIBWO is a novel variant of the conventional relativistic BWO, operating at electron energies of $\gtrsim 500keV$. The concept originated in work conducted at the Institute of High Current Electronics (IHCE) Russia at ~3GHz [1,2]. A variation of the concept was investigated, at X-band, at the National University of Defense Technology (NUDT) China [3]. Over the same time period the UoS undertook an investigation of an S-band SIBWO variant, with results presented at the 2015 Joint UK / US Directed Energy Workshop [4]. The current work involves the development of an X-band variant of the UoS work, shown in schematic cross-section in Figure 1.1.

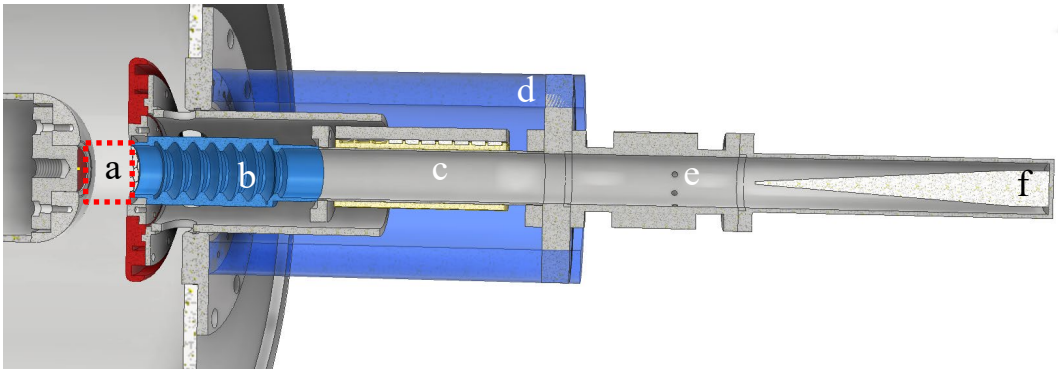

Figure 1.1. Schematic cross-section of SIBWO prototype assembly noting (a) A-K gap of accelerating diode (b) interaction region (c) beam dump (d) linear-stage location for A-K gap adjustment (e) field probe diagnostics (f) attenuating load termination

This includes the incorporation of klystron-like elements to enhance efficiency [5 – 10], though the dominant characteristics remain BWO-like. Results from the project have been presented at conferences [11 – 15].

The key components of Figure 1.1 will be discussed in the following sub-sections.

1.4.1 Accelerating Diode

The accelerating diode of the SIBWO is shown in schematic cross-section in Figure 1.2.

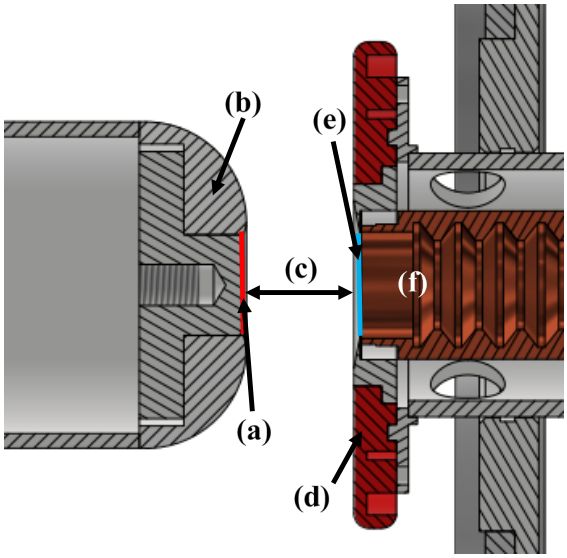

Figure 1.2. Schematic cross-section of the SIBWO accelerating diode, noting key aspects (a) the emitter region, (b) cathodic focus electrode, (c)A-K gap, (d) movable anode-face, (e) anode-grid plane, (f) location of SIBWO interaction region.

It was comprised of an electron emitter (Figure 1.2(a)), of typically $16mm$ radius, surrounded by a field-shaping cathodic focus electrode (Figure 1.2(b)) curving out to the cathode stalk radius of $50mm$. The accelerating gap (anode-cathode, or A-K gap, Figure 1.2(c)) was typically $25mm$, though this could be adjusted as required. A sparse metallic grid (Figure 1.2(e)) was positioned to provide the effective anode-plane of the A-K gap and provide electromagnetic (EM) isolation between the diode and interaction (Figure 1.2(f)) regions.

The current emitted is a function of the diode geometry, known as the Perveance ($\mathcal{P}$), relating to the applied potential as:

$$\mathcal{P} = \frac{I}{V^{3/2}} \tag{1}$$

Where V is the applied potential, I is the emitted current and $\mathcal{P}$ is typically expressed in 'micropervs'.

Calculation of $\mathcal{P}$ for a realistic diode is best performed via numerical modeling, with experimental measurement used for verification. Provided there is no change of operational state (e.g. meeting different emission thresholds in the diode materials), once the emitted current is known for a given accelerating potential it is possible to predict the emitted current at arbitrary potential using (1). This makes determination of $\mathcal{P}$, and tracking its value as a function of V, a useful parameter in characterizing the operation of an accelerating diode over its intended operational range.

An important note, especially in relation to a self-insulating source such as the SIBWO, is consideration of how I is measured. In a conventional BWO the EM isolation between the diode and interaction regions is typically obtained through the use of a step-reflector, meaning there is no physical impediment to the (externally magnetically constrained) electron beam as it propagates between regions. The transmitted current is then collected using a Faraday-cup for measurement, which in this case maps directly to the total emitted current.

In the SIBWO, as the EM isolation of the diode and interaction regions is provided by a sparse metallic grid, some portion of the emitted current is intercepted by the grid, meaning the Faraday-cup collected current is lower than the total emitted current. In addition, as the beam is propagating only under the influence of its own self-forces it will be naturally divergent, becoming more-so at lower applied potentials. This may be quantified by consideration of the Lorentz force:

$$F_L = -e(E_r + v_z \times B_\theta) \tag{2}$$

Where $e = 1.60 \times 10^{-19}\ C$ is the electron charge, E_r is the particle self-radial-Electric field, B_θ is the corresponding self-azimuthal-Magnetic field and v_z is the axial particle velocity.

The net force F_L in (2) causes the electron beam to diverge radially as it propagates due to the radially outward force $-eE_r$, that is offered only partial mitigation by the radially inward (pinching) force $-e(v_z \times B_\theta)$. The effect of this radial divergence being interception of a portion of the electron beam on the anode face (Figure 1.2(d)) when the beam cross-section exceeds that of the anode-grid at the transmission plane. The magnitude of this radial divergence decreases with increasing applied potential in accordance with the laws of Special Relativity. The 'self-insulated' transport of the electron beam through the SWS interaction region is also aided by the use of higher applied potentials for the same reason. SIBWO designs therefore benefit from the use of comparatively high applied potentials.

For a chosen applied potential V, adjusting the A-K gap, (provided it is the dominant geometric factor in determining $\mathcal{P}$) allows the desired magnitude of the electron beam current I, determined by equation (1), to flow through the diode. This also requires the electric field E in the A-K gap to be sufficiently large to produce electron emission from the intended central emitter region on the cathode. However one must be aware of the effects of increased E-field stresses on the diode's other components. If one exceeds the emission threshold of the focus electrode surface any electrons emitted from here are most likely to transit the A-K gap, terminating on the anode-face – indeed such unintended emission can impact on emission from the intended emitter.

To properly monitor the total emission in the diode it is therefore desirable to measure the current flowing in the cathode stalk (I_{tot}), as well as that transmitted into the interaction region (I_{SWS}). As the former relates to the efficiency of the source as a whole, while the latter relates to the electronic efficiency of the interaction region between the transmitted beam and the EM-field. From previous experience at the UoS, I_{SWS} tends to follow the trend predicted by equation (1) as V is varied, essentially giving a scaling parameter $\mathcal{P}_{SWS}$ for determining current at arbitrary V. Monitoring of I_{tot} then allows for calculation of $\mathcal{P}$ proper, quantification of the percentage loss of the electron beam, and provides a means of detecting changes in diode operation (e.g. emission from the focus electrode).

The SIBWO diode was designed to provide $\sim 2kA$ of current at an applied potential of $\sim 500kV$.

1.4.2 SIBWO Interaction Region

The interaction region (Figure 1.1(b)) is shown in detailed cross-section in Figure 1.3.

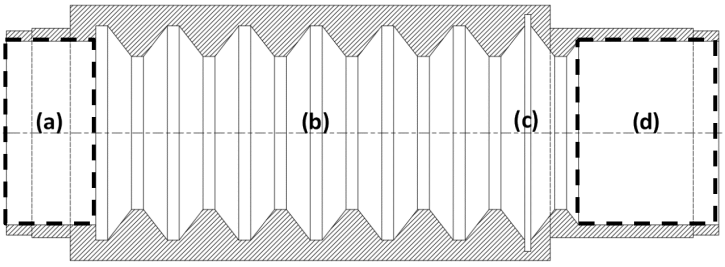

Figure 1.3. Schematic cross-section of the SIBWO interaction region noting key aspects (a) lead-in modulating cavity, (b) periodic trapezoidal slow-wave structure (SWS), (c) Klystron-like resonator (d) SWS exit

The mean radius of the interaction region was $r_0 = 18mm$, with an initial $d_{zmod} = 17.5mm$ long lead-in section (Figure 1.3(a)) functioning as a pre-modulation cavity, defined between the grid boundary and the transition into the Slow-Wave Structure (SWS, Figure 1.3(b)). The SWS was formed of 6 regular trapezoidal periods, with a periodicity of $d_z = 14mm$ and amplitude $r_1 = \pm 3mm$. Such a SWS closely approximates the performance of a truly sinusoidal structure, typically defined as:

$$r = r_0 + r_1 \cos(h_z z + M\theta) \tag{3}$$

where $h_z = 2\pi/d_z$ and M is the azimuthal index (number of half-period variations) of the structure. For the SIBWO $M = 0$ but the condition should not be ignored.

As the electron beam propagates through this structure, naturally radiating broad-band noise in all supported EM field structures and in both longitudinal directions, a portion of said noise is "scattered" in a periodic fashion by the modulation of the fields induced by the SWS. Coupling then occurs between the counter propagating waves of any two field patterns that satisfy the Bragg resonance conditions

$$h_z = k_{z+} + k_{z-} \tag{4.1}$$

$$M = M_+ + M_- \tag{4.2}$$

where the $+/-$ notation denotes properties associated with wave propagating in the forward and backward longitudinal directions.

This produces a series of "eigenmodes"; EM field structures that only exist within the bounds of the SWS and with which the propagating electron beam may interact. The TM_{01} eigenmode for the SIBWO SWS is shown in Figure 1.4, along with representation of the e-beam's Slow-Space-Charge-Wave to indicate the expected resonant frequency as being $\sim 9.4GHz$ for the beam parameters indicated.

Following the six regular periods of SWS a discontinuity was introduced (Figure 1.3(c)). The inclusion of such discontinuities provides a means of adjusting the relative phase of the EM field to that of the propagating electron beam.

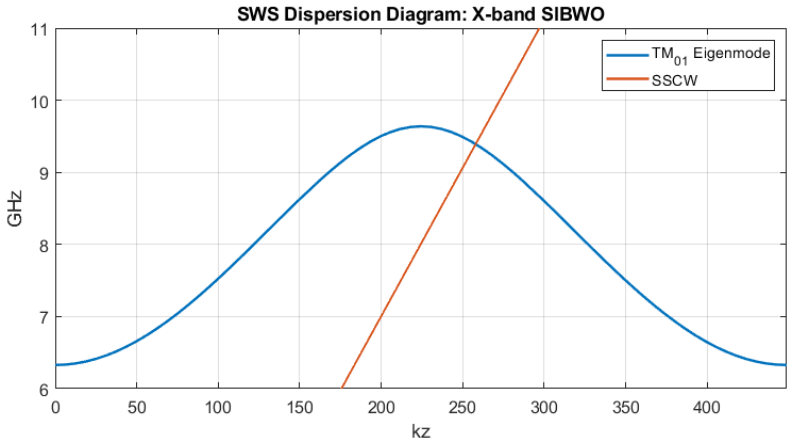

Figure 1.4. Shows the dispersion curve of the TM_{01} mode in the SIBWO SWS, along with the e-beam SSCW, indicating resonance at $\sim 9.4GHz$ for a $500keV, 2kA$ e-beam.

This allows for additional modulation and feed-back at a frequency set by the discontinuity's dimensions and its location within the SWS- essentially it forms an additional narrow-band resonator within the body of the SWS proper. In the SIBWO prototype, the location of this additional resonant structure, towards the end of the SWS, primarily provides a means of enhancing the modulation at a set frequency, with its dimensions adjusted (along with the initial modulating cavities length) to overlap within the resonant bandwidth of the main interaction of the SWS and the e-beam. The resonator dimensions were $d_{zres} = 1.2mm, r_{res} = 46.4mm$. The SWS was then terminated back at the mean radius as shown, with the output waveguide again at $r_0 = 18mm$. Numerical predictions for the performance, when driven by the e-beam generated in the accelerating diode model, indicated output powers of $\sim 220MW$, at $\eta \sim 25\%$.

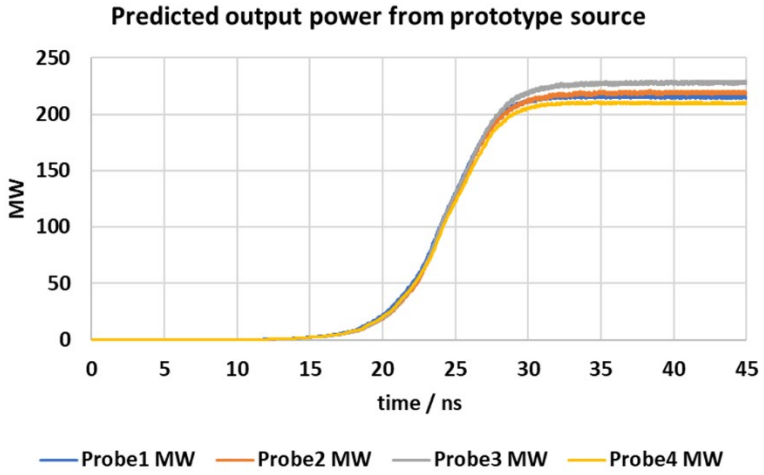

Figure 1.5. Output power envelopes predicted in CST Particle Studio for prototype SIBWO design. Traced taken from four probes designed as described in Section 1.4.4.

The corresponding output spectra are shown in Figure 1.6.

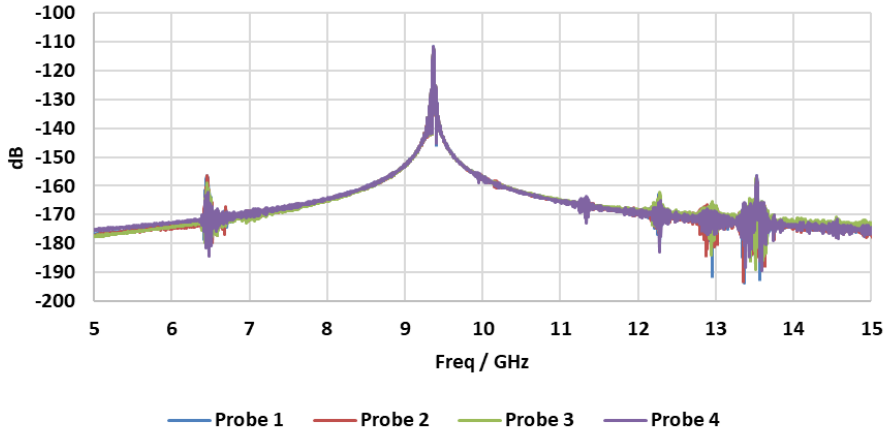

Figure 1.6. Shows the predicted spectral content of the SIBWO output, sampled across four field-probes.

The dominant resonant frequency was $\sim 9.4GHz$ for a $500keV, \sim 2kA$ electron beam, in-line with the theoretical value shown in Figure 1.4. The frequency "lock" provided by the discontinuity in the SWS was predicted to make the SIBWO very robust to variation in the beam parameters.

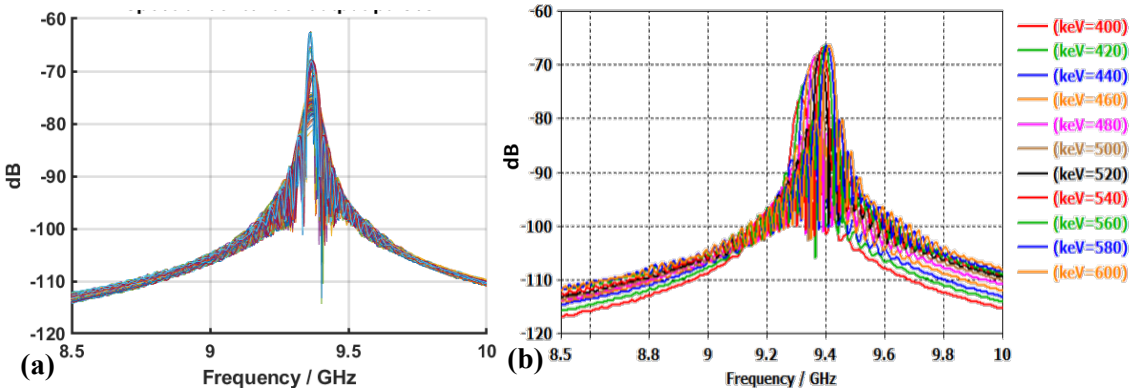

Figure 1.7. Shows change in the spectral output (a) at a mean beam energy of $500keV$ with the energy spread varied up to 10%, up to 2% angular spread and beam "fill-factors of $80-100\%$ (b) variation in the mean energy from $400-600keV$ with the beam current scaling as given by equation (1).

Figure 1.7 shows the change in dominant resonance with significant variation in the electron beam parameters. While the output power reduced as the beam parameters moved away from the optimized condition at $500keV, \sim 2kA$, the output power remained HPM across the ranges indicated, with the resonant frequency showing a maximum shift of $\sim 100MHz$ after a 20% reduction in beam energy.

1.4.3 Beam dump

At the time of writing UK regulations, regarding the radiation of radio and microwave frequency signals, were such that it was decided the most effective way of determining the output from the SIBWO was through the use of a series of field-probes, with the majority of the output depositing in a high-power load termination. Given the divergent nature of the electron beam it was anticipated that electron deposition would occur throughout the length of the SWS and indeed for some distance beyond, meaning one must therefore remove any remnants of the beam prior to detection of the output wave pattern, as the incidence of high-energy electrons on a field-probe, the absorbing load, or indeed a vacuum window, would risk significant component damage.

To account for this in the prototype an electron beam-dump was positioned some distance beyond the exit from the SWS. The dump was formed by a set of readily available Samarium Cobalt rare-earth magnets, mounted as shown in Figure 1.8. The exact position of the dump was not critical, with the only consideration being prevention of any meaningful physical overlap between the applied magnetic field and the interaction region; the action of the dump should in no-way impact on the operation of the SIBWO, or invalidate its self-insulating aspect.

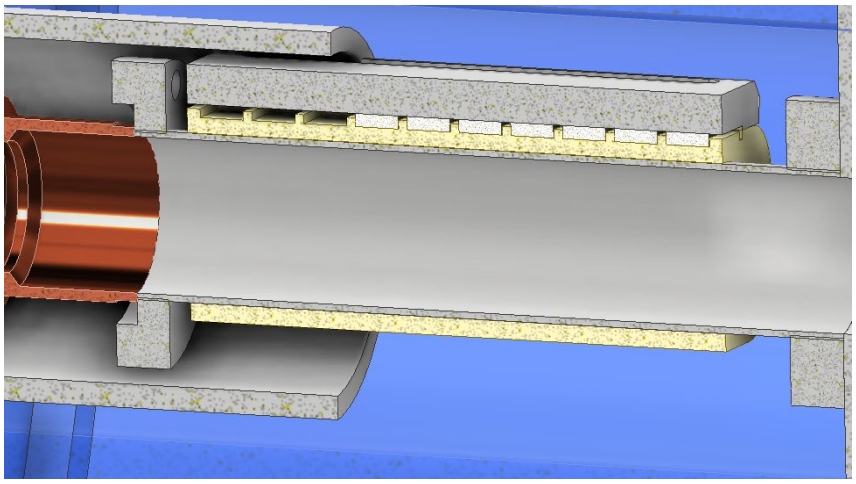

Figure 1.8 Schematic cross-section of the beam-dump, showing a series of 10 discrete Samarium Cobalt bar magnets arranged in a manner that redirects any electrons propagating through to the opposing side of the waveguide wall.

The beam dump was $125mm$ in length, with the internal radius maintained at $r_0 = 18mm$. The magnets were Samarium Cobalt grade Sm_2Co_{17} (remnant magnetization $\sim 1T$), providing an on-axis transverse field strength of $\sim 15mT$ through the bulk of the dump section.

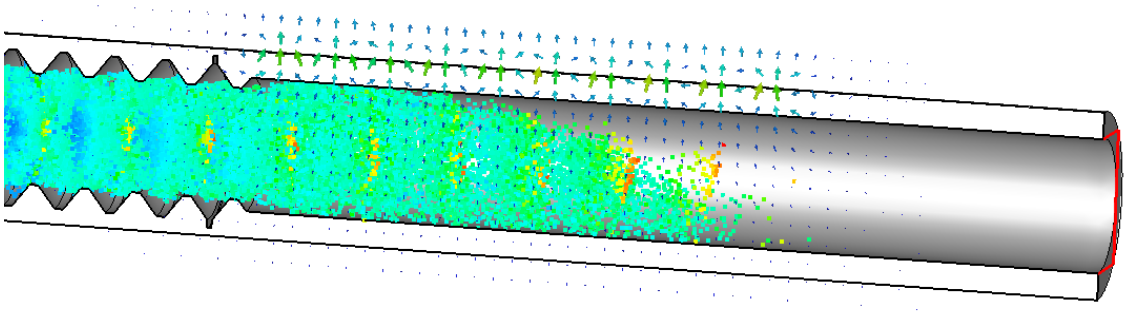

Figure 1.9. Shows the particle trajectories predicted in CST Particle Studio for the SIBWO model incorporating the beam-dump magnetic field.

This was predicted to be sufficient to remove the remaining electron beam via numerical modeling in CST studio. No impact on the operation of the SIBWO was predicted for a beam dump positioned as indicated above.

1.4.4 Output Field-Probe diagnostic

The field-probe assembly can be seen in Figure 1.10. It comprised two sets of E-field probes, distributed around the azimuth of the output waveguide as shown, with the axial separation distance between sets being $36mm$.

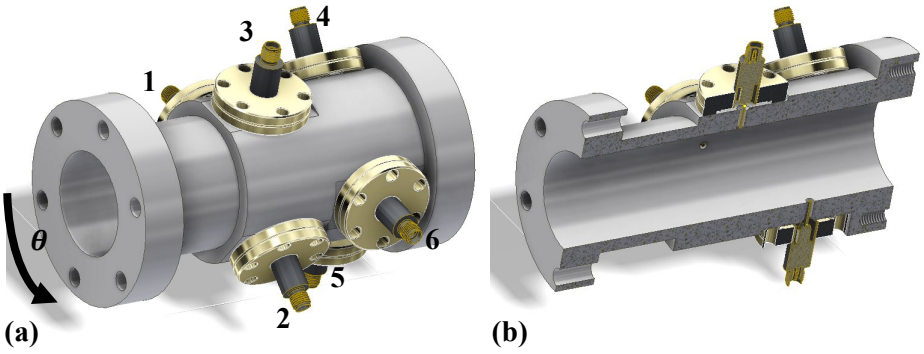

Figure 1.10. Shows the SIBWO output diagnostic, formed of six E-field probes, distributed across two sets of three probes as shown in (a). (b) shows the diagnostic in cross-section. Set 1 included probes 1 – 3 at $\theta = 0, 3\pi/4, 3\pi/2$, Set 2 included probes 4 – 6 at $\theta = \pi/2, \pi, 7\pi/4$.

The closest resonance within the SIBWO to the intended TM_{01} outputs is the TE_{11} (from an HE_{11} interaction). If one assumes a waveform composed of a linear TE_{11} signal co-propagating with a TM_{01} signal, a given probe signal will follow:

$$A_n = A_{TE}\cos(\theta_n - \Delta\theta)\cos(\omega_{TE}t - \Delta\phi_{TE}) + A_{TM}\cos(\omega_{TM}t - \Delta\phi_{TM}) \quad (5)$$

where $A_{n,TE,TM}$ are the peak amplitudes of the recorded, TE and TM waves at probe n (respectively), θ_n is the azimuthal position of the probe, $\Delta\theta$ is the angular displacement of the TE_{11}

peak-of-field (POF) relative to $\theta = 0$ and $\omega_{TE,TM}$ are the frequencies of the TE and TM signals. The $\Delta\phi_{TE,TM}$ terms account for the arbitrary starting phases of the different modes.

From this it can be seen that the measured contribution from the TE_{11} wave depends on the azimuthal position of the probe and the relative position of the POF, while the contribution from the TM_{01} wave is independent of the probe's azimuthal location. The arrangement of probe in Figure 1.10 therefore allows for quick determination of the operating mode through comparison of signal magnitude and relative phase across a given probe-set. Where the TM_{01} resonance is clearly dominant all probes should report identical waveforms (within experimental error), while any notable presence of the TE_{11} (or other azi-asymmetric) mode will be evident in variation in the reported magnitudes and phases. In either case, given typically $\omega_{TE} \neq \omega_{TM}$, it is relatively trivial to extract the TE_{11} and TM_{01} AC waveforms for each probe through suitable spectral windowing in Fourier analysis. The magnitude of the TE_{11} component can then be determined by solving (5) across a given probe-set for $\Delta\theta$ and scaling the recovered TE_{11} waveforms accordingly.

Where the TE_{11} component is not linearly polarized (5) is modified as

$$A_n = A'_{te1}\cos(\theta_n - \Delta\theta) + A'_{te2}\sin(\theta_n - \Delta\theta) + A_{TM}\cos(\omega_{TM}t - \Delta\phi_{TM}) \qquad (6)$$

where $A'_{te1,te2} = A_{te1,te2}\cos\left(\omega_{TE}t - \Delta\phi_{te1,te2}\right)$ and $\Delta\phi_{te1} \neq \Delta\phi_{te2}$.

Provided $\omega_{TE} \neq \omega_{TM}$ the contributions from the degenerate, orthogonal TE_{11} partial-modes can be determined as before, by applying (6) across a given set of probe signals and solving for the relevant parameters (noting in both of the above cases any contributions from the mode are removed during the Fourier analysis step).

Where two co-propagating modes do so at like frequency ($\omega_{TE} = \omega_{TM}$) one cannot separate the constituent AC waveforms via Fourier analysis. In this case, provided a sufficient number of probes is included in a given probe-set, it is possible to recover said waveforms by the same method of applying (5) or (6) to each signal from a probe-set, then solving for $A_{TE,TM}$ and $\Delta\theta$. A set of three probes per set was deemed sufficient to cover the potential modes of operation from the SIBWO.

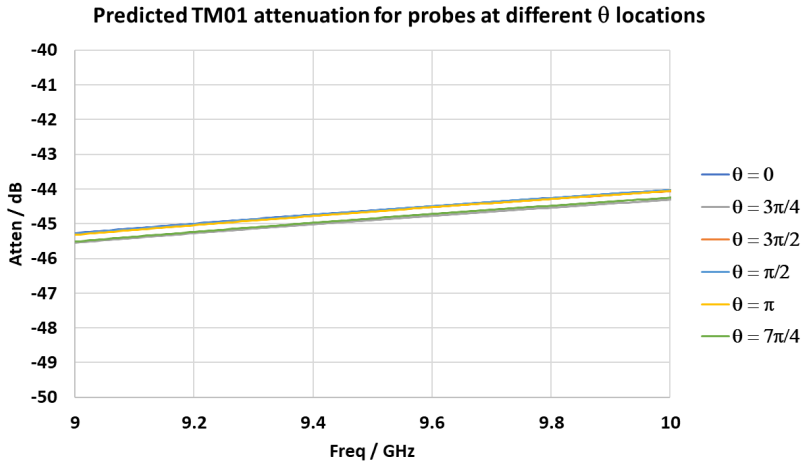

Figure 1.11. Predicted attenuations for the different probes in the diagnostic.

Modeling of the diagnostic indicated the probes would couple $\sim -45dB$ of the propagating signal. Taking a maximum output power of $300MW$ (around the maximum achieved numerically for the SIBWO when driven with an idealized electron beam) this corresponds to $\sim 10kW$ coupled by the probes, or $\sim 700V$ on the line; well within the operational limits of the SMA connectors and the coaxial lines used to connect the diagnostic to the measuring oscilloscope (with additional attenuation from the lines adding at least a further $5dB$ prior to measurement of the scope). Coupling of the TE_{11} and TE_{21} modes was predicted to be of similar magnitudes, within $1dB$ of that predicted for the TM_{01}, i.e. within the error margin of the experiment.

1.4.5 Load Termination

The load termination for the SIBWO was required to have high power handling and show low reflection. The design was developed with input from Thorndike Corp [16], taking the form of a poly-iron high-power cone-load with material properties close to those listed in CST for ECCOSORB MF-110.

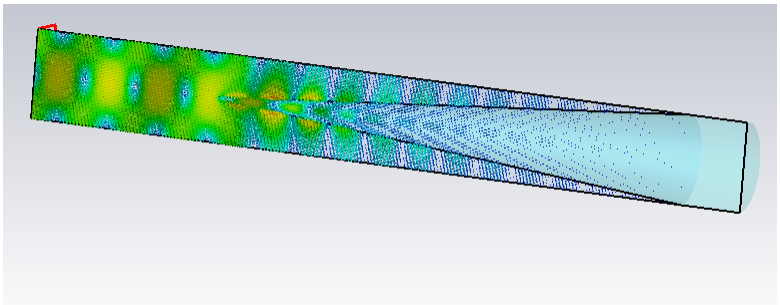

Figure 1.12. Cross-section of the load model showing attenuation of a TM_{01} signal

The predicted reflection from the load was $\sim -43dB$ down on the incident signal magnitude, corresponding to $\sim 0.5\%$ of the incident power being fed back into the source. Numerical modeling of the SIWBO including the load showed no notable impact on performance from this level of feedback.

1.5 References

1. Totmeninov, E.M. et al., 2009, *IEEE Trans. Plasma Sci.*, **37(7)**, pp. 1242 – 1245.
2. Totmeninov, E.M., et al., 2011, *IEEE Trans. Plasma Sci.*, **39(4)**, pp. 1150 – 1153.
3. Guo, L.M., et al., 2017, *Rev. Sci. Instrum.*, **88(2)**, article 024708.
4. MacInnes, P., et al., 2015, 15-19 June *2015 UK / US Directed Energy Workshop, Swindon, UK.*
5. Phelps, A.D.R., 2018, *ONR HPM Program FY 2018 Report.*
6. Phelps, A.D.R., 2019, *ONR HPM RPPR 2019.*
7. Phelps, A.D.R., 2019, *ONR HPM Program FY 2019 Report.*
8. Phelps, A.D.R. 2020, *ONR, HPM RPPR 2020.*
9. Phelps, A.D.R. 2021, *ONR, HPM Program FY 2020 Report.*
10. Phelps, A.D.R. 2021, *ONR, HPM RPPR 2021.*
11. MacInnes. P., et al., 2019, *UK / US Directed Energy Workshop, Swindon, UK,* 22-26 July 2019.
12. MacInnes, P., et al., 2020, *47th Int. Conf. on Plasma Sci. (ICOPS 2020),* 6-10 Dec. 2020.
13. Crampsey, B., et al., 2020, *47th Int. Conf. on Plasma Sci. (ICOPS 2020),* 6-10 Dec. 2020.
14. MacInnes, P., et al., 2021, *UK Institute of Physics, 47th Plasma Physics Conference,* 6-9 April 2021.
15. MacInnes, P. et al., 2022, *UK/ US Directed Energy Workshop, Swindon, UK*, 18-22 July 2022.
16. Thorndike Corporation, website: https://thorndikecorp.com/

2. Experimental Assembly and Calibration

2.1 Pulsed Power Supply:

The UoS possesses a relatively long-pulse ($200 - 250ns$) single-shot pulsed power supply, driven by an inverting Marx-bank generator discharging to a deionized-water-filled pulse-forming transmission line [1].

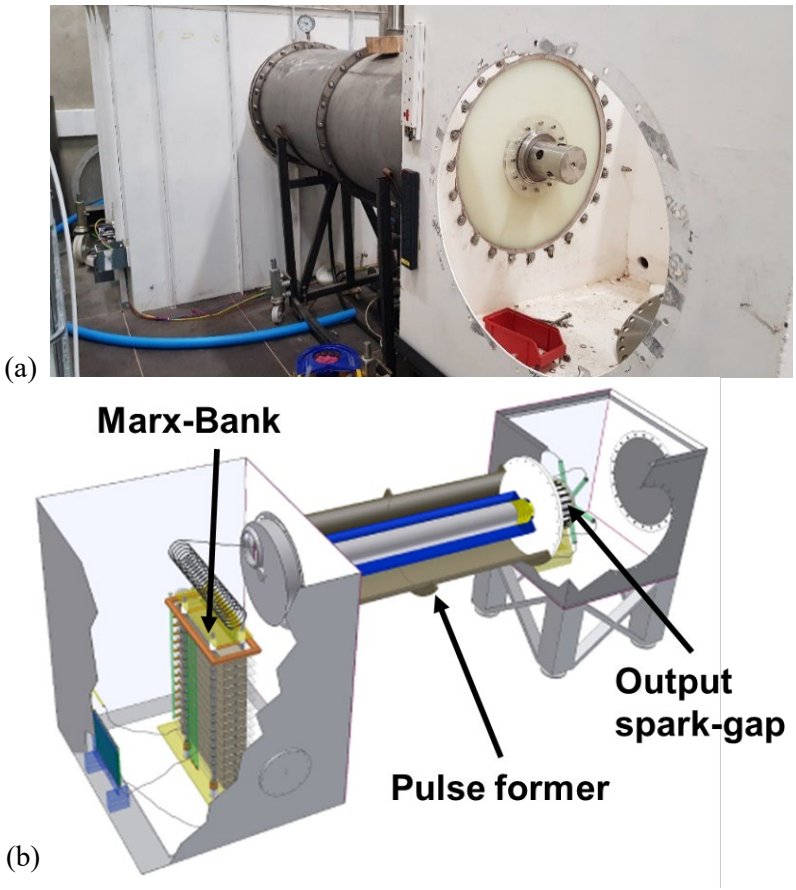

Figure 2.1. Shows (a) the physical Pulsed Power Supply (PPS), (b) a schematic of the PPS showing key assembly details.

The Marx-bank consisted of a set of fifteen Maxwell (latterly General Atomic) $0.3\mu F$ capacitors, rated as providing a maximum of $100kV, 25kA$ each. This gives a maximum output from the bank of $1.5MV$ at $25kA$ ($22.5kJ$ max). The Marx discharged to a folded transmission line (electrically appearing as a standard transmission line double the physical length) terminated in a high-voltage spark-gap. The output could be controlled by varying the pressure in the spark-gap to ensure closure at the peak of the charging cycle from the Marx. The line discharged to a deliberately mismatched load termination ($\sim 15\Omega$ against the $\sim 5\Omega$ of the transmission line) as this provided $\sim 2/3$ of the peak Marx discharge voltage across the load termination. While this results in a stepped discharge (see Figure 2.2) the voltage at which this occurs is outside the operational bandwidth of the source.

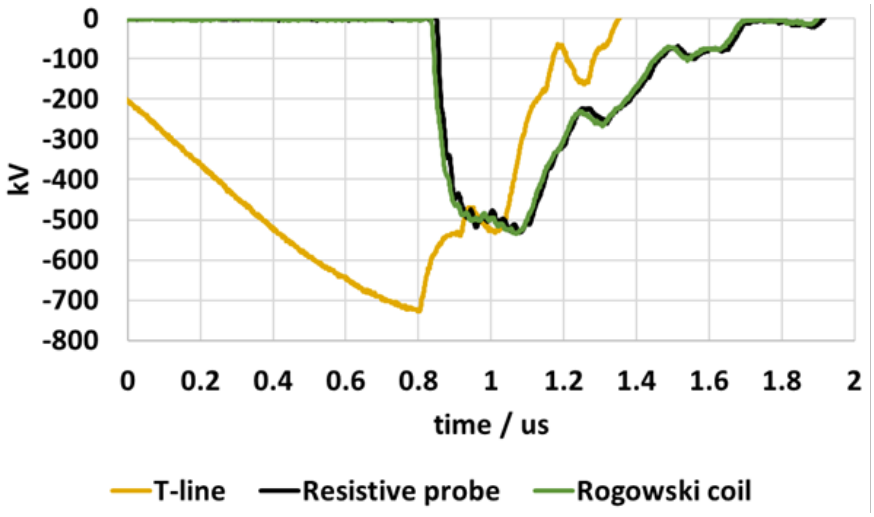

Figure 2.2: Shows an example of the output from the pulsed power supply. Three diagnostics were employed, a D-dot probe at the output of the pulse forming transmission-line (T-line), a resistive probe in parallel with the dummy load and a Rogowski coil reading the current flowing to ground from the load.

The minimum firing voltage of the PPS is $\sim 360kV$, while the potential maximum (as configured) is $\sim 1MV$; typical output pulses fall in the range $400 - 600kV$.

The performance of the PPS, discharging into the load termination with a dummy load approximating the impedance of the SIBWO acceleration diode placed in parallel, was monitored by a set of integrated diagnostics. A D-dot field probe (capacitive pick-up probe) at the output of the pulse forming line monitored its charging and discharge cycle, as can be seen in Figure 2.2 (the dip in the associated trace represents the closure of the output spark-gap). The output pulse was then monitored by a resistive probe, placed in parallel with the load, and a Rogowski coil, placed around the current path from the load to ground. The charging voltage on the Marx capacitors, for the shot shown in Figure 2.2, was $50kV$, giving a total discharge voltage of $\sim 750kV$. The voltage applied across the output load was then $\sim 500kV$, confirming the $3{:}\,1$ impedance mismatch between the load termination and the impedance of the line. Peak output was maintained for $\sim 250ns$.

2.2 Accelerating Diode:

The accelerating diode (Section 1.4.1) was designed to provide an electron beam at $500keV, \sim 2kA$ corresponding to a diode impedance of $\sim 250\Omega$. The assembly of the accelerating diode can be seen in Figure 2.3(a), with the diode under vacuum shown in Figure 2.3(b). Vacuum was maintained in the low $10^{-6}mbar$ range.

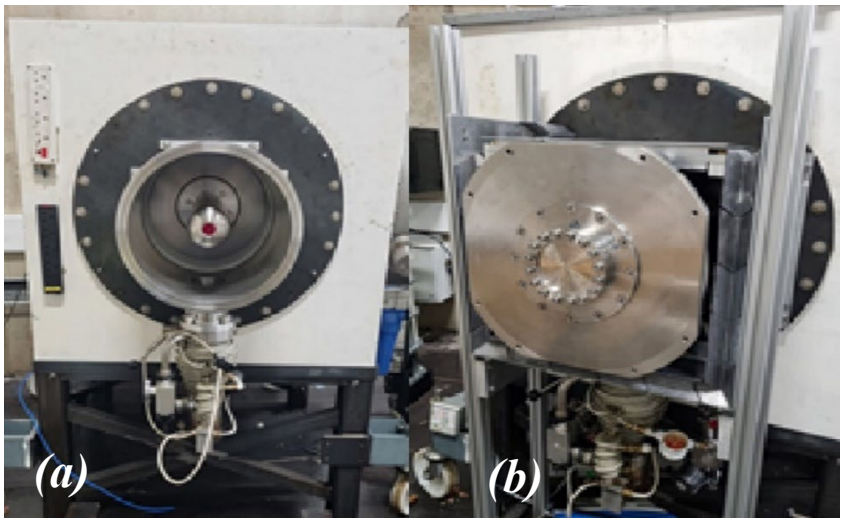

Figure 2.3: (a) The accelerating diode, showing the internal cathode stalk assembly, (b) the accelerating diode under vacuum.

The bounding anode vessel diameter was $400mm$, surrounding a cathode stalk of diameter $100mm$. This was to maximize ease of access in the prototype source; a more developed variant could reduce these sizes significantly.

2.3 Interaction Region Assembly

The interaction region was constructed in-house using a CNC lathe to machine an aluminum former (Figure 2.4(a)) which was then electroplated with copper to a thickness of $\sim 3mm$ (Figure 2.4(b)). The aluminum was then dissolved, with the copper machined to length prior to cold testing (Figure 2.4(c)).

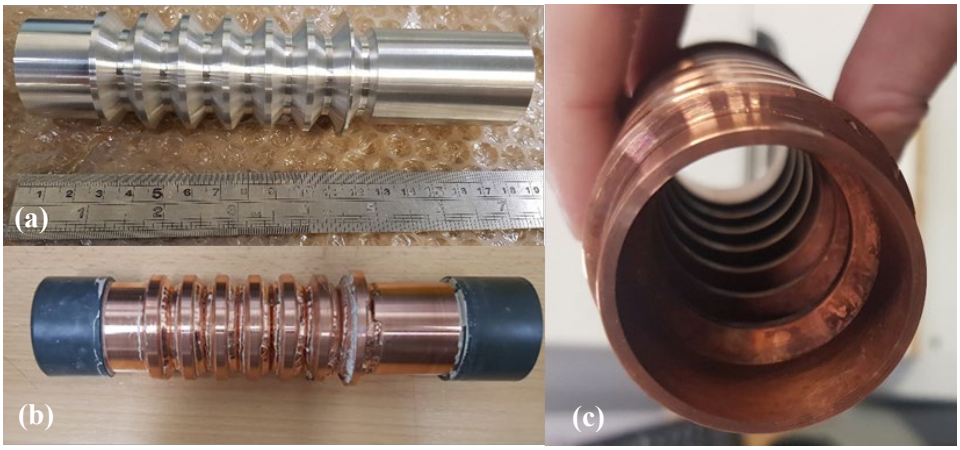

Figure 2.4. Shows (a) the aluminum former of the SWS, (b) the former after electrodeposition of copper, (c) the SWS obtained after removal of the aluminum.

The cold test assembly for the interaction region is shown in Figure 2.5(a).

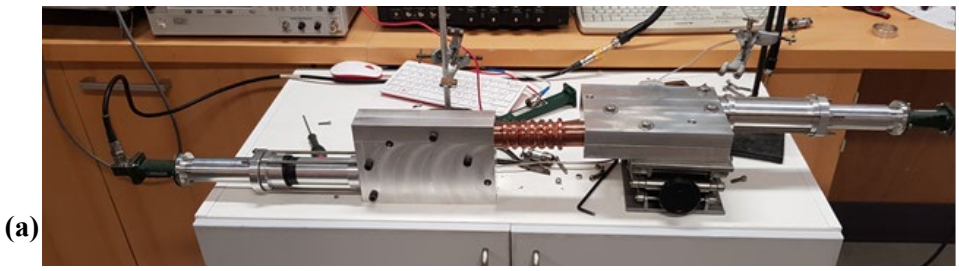

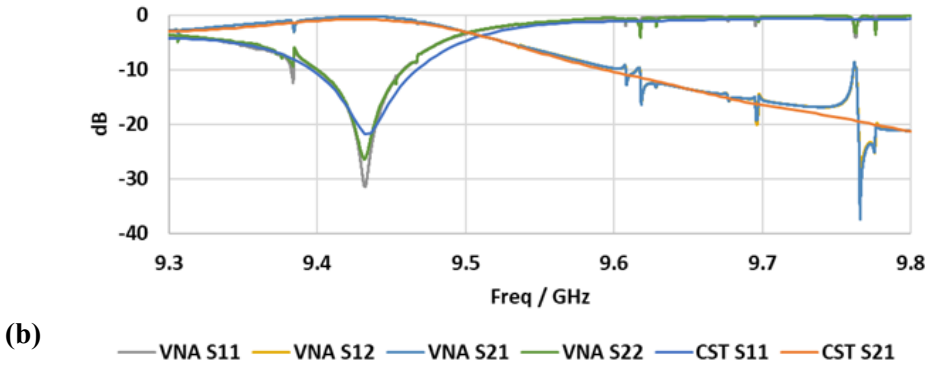

Figure 2.5. Shows (a) the cold-test assembly of the interaction region, (b) the measured S-parameters compared with numerical prediction.

An Anritsu MS4647A Vector Network Analyzer (VNA) was calibrated using standard rectangular WG16 waveguide, with the initial TE_{10} mode of the rectangular guide converted to linearly polarized TE_{11} via a rectangular to circular taper. This was then converted to the desired TM_{01} mode using a serpentine, with the conversion process reversed at the exit of the interaction region. The serpentines were designed to provide efficient TE_{11} – TM_{01} conversion over the range $9.3 - 9.8GHz$, with the expected SIBWO operating frequency to be $\sim 9.4GHz$. Excellent agreement can be seen between the measured and predicted cold performance. In regards to the periodic distortions in the measured results, it should be noted the serpentine (as with any) mode converter was not 100% efficient, with the net result being the formation of cavity resonances within the system. It was found rotating the input and output converters such that the initial WG16 sections were cross-polarized provided best mitigation of such effects, providing the curves shown in Figure 2.5(b).

The interaction region was then placed within the experimental assembly, as shown in Figure 2.6 with the interaction region and beam-dump under vacuum within the linear stage.

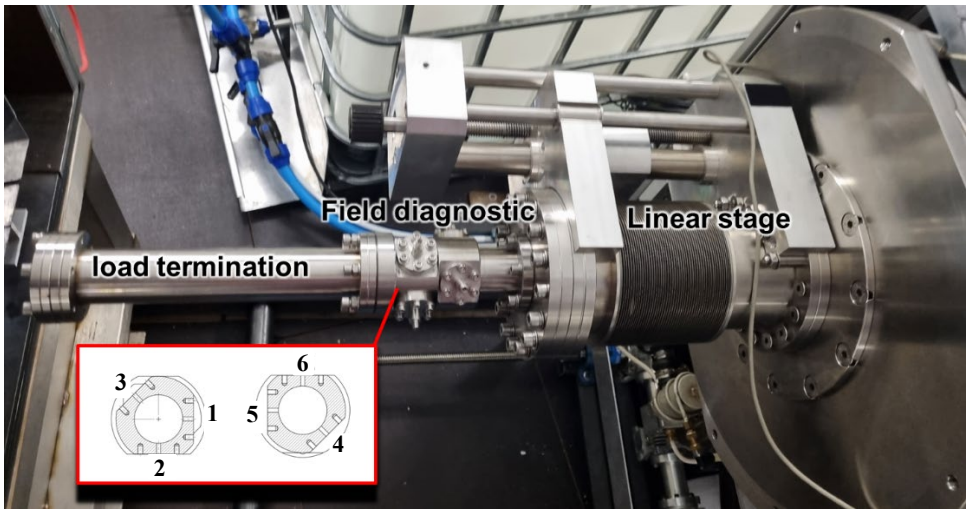

Figure 2.6. Shows the experimental assembly of the SIBWO, noting the location of the field diagnostic and load termination. The beam dump and interaction region were located within the linear stage.

2.4 Beam dump assembly

The Beam dump was formed by a set of ten Sm_2Co_{17} Samarium Cobalt rare-earth bar-magnets, set in a line above a length of regular stainless-steel cylindrical waveguide ($r_0 = 18mm$). Their movement was constrained using a nylon former, held in place with A4 stainless steel bolts.

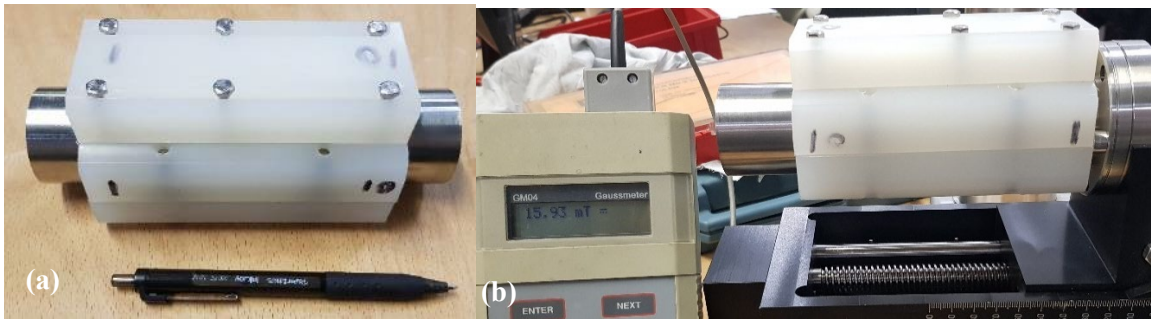

Figure 2.7. Shows (a) the assembled beam dump, (b) testing of the magnetic field profile.

The magnetic field profile was measured along the central axis, using both an axial and a transverse field probe; Figure 2.7(b) shows a measurement of the transverse field near the middle of the dump section. The measured B-field was compared against that predicted by CST Microwave Studio as shown in Figure 2.8.

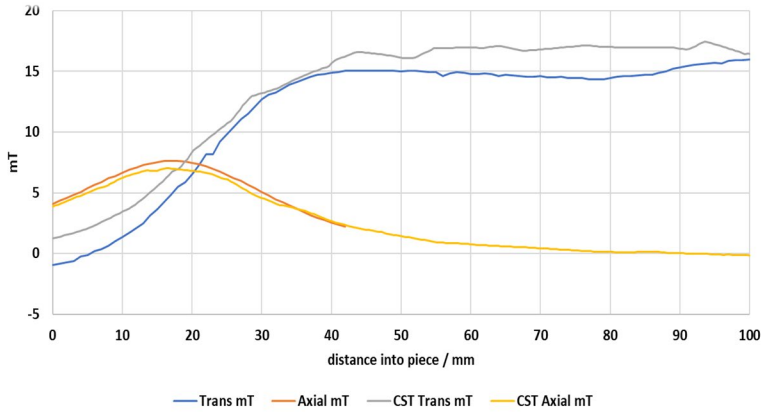

Figure 2.8. Shows the predicted and measured magnetic field profile for the beam dump.

This showed very good agreement with prediction. The difference observed in the peak amplitude of the transverse field, between prediction and experiment, was attributed to physical "sag" in the transverse field probe, resulting it the probe tip lying slightly low and off-axis during the measurement. Adjusting the numerical diagnostic position to follow this assumption reproduced the measured reduction in the transverse field profile.

Figure 2.8 shows the extent of the field profiles that could be measured, given the lengths of the probes, without disassembly and re-orientation of the setup. As the key concern was determination

of the field profile into the bulk of the magnet assembly this was not performed. The agreement shown was considered sufficient to validate the dump should work as intended for the expected electron energies present in the SIBWO.

2.5 Field Diagnostics

The output field diagnostic was machined from 316L stainless steel, with integrated standard CF70 flanging. The CF35 flanging, of the SMA vacuum feedthroughs, allowed for a maximum of three probes in each probe-set, located as described in Section 1.4.4. The diagnostic is shown in Figure 2.9, along with a variety of mode converters used to launch different modes / mode mixtures.

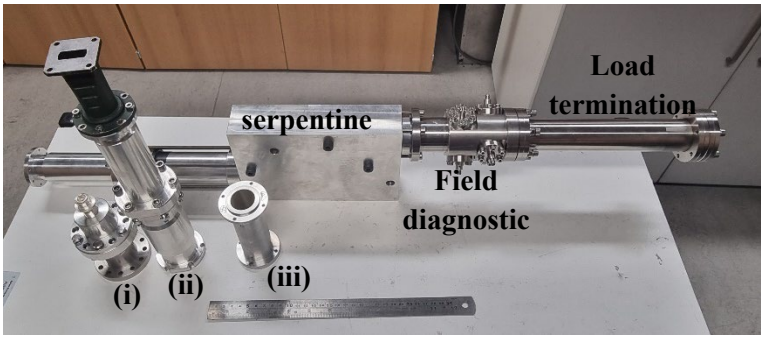

Figure 2.9. Shows the field diagnostic connected to a serpentine ($TE_{11} - TM_{01}$) mode converter, along with converters to launch (i) TM_{01} directly (ii) linear TE_{11} (iii) TE_{11} circular polarizer.

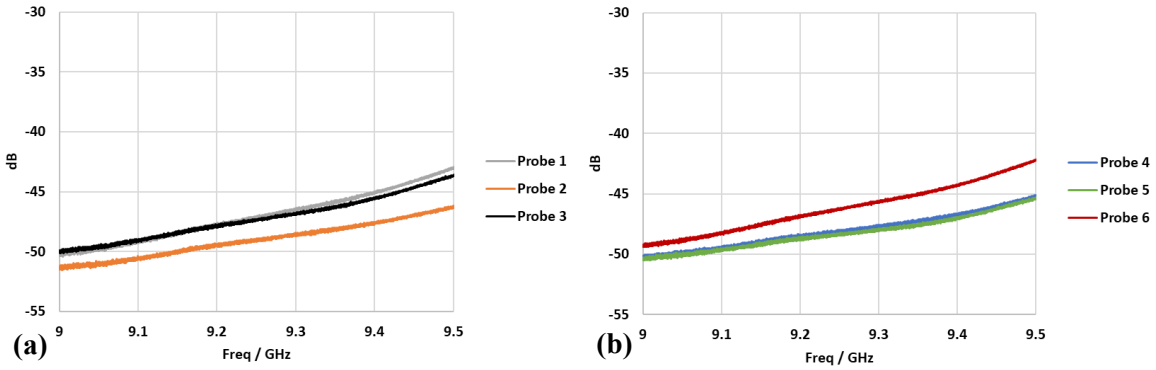

Figure 2.10. Shows the measured attenuations for the probes, separated by probe-set. (a) probes in set 1, probes 1 – 3 at $\theta = 0, 3\pi/4, 3\pi/2$ (b) probes in set 2, probes 4 – 6 at $\theta = \pi/2, \pi, 7\pi/4$.

Figure 2.10 shows the measured attenuations of the probes, obtained using a coaxially launched TM_{01} signal (Figure 2.9(i)). Inter-probe variation was expected, as the attenuation offered is a function of the penetration depth of the feedthrough pin (essentially the "probe") into the waveguide body and the variation in pin length was on the order of $\pm\, 0.2mm$. This was measured prior to machining of the diagnostic body, with the location of the vacuum flanging planes set such that the longest probe "tip" should sit at the mean radius of the internal wall; i.e. none of the probe tips should protrude into the waveguide body. Comparing Figure 2.10 and Figure 1.11 it can be seen

that the measured performance was at least as good as prediction, with the attenuations being $\sim -45dB$ or better in the region of the expected resonant frequency $9.4GHz$.

2.6 Load Termination

The load termination is shown in Figure 2.11. It was manufactured by Thorndike Corp, MA, USA, from TC2000 poly-iron (an in-house material with equivalent material parameters to ECCOSORB MF-110).

Figure 2.11. Shows (a) the high-power cone load, (b) the load fitted within the experimental assembly.

The performance of the load was calibrated as shown in Figure 2.12.

Figure 2.12. Shows the cold-test assembly for characterizing the load termination.

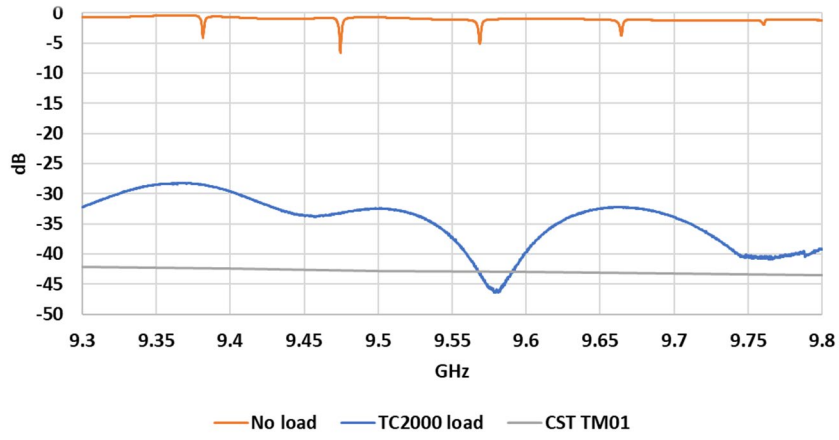

Figure 2.13. Shows the predicted and measured performance of the SIBWO load termination.

The reflection predicted by CST Microwave Studio was $\sim -43dB$ at $\sim 9.4GHz$, while the measured reflection was $\sim -30dB$. Investigation of this, by varying the insertion length of the load (see the open-ended fitment in Figure 2.12) and by replacement with an alternative wooden load, showed the reflected signal to be dominated by the transitions between components prior to the section holding the load itself. The performance of the load should therefore be seen as being at least as good as indicated in Figure 2.13, with the actual performance likely more in-line with prediction. This was considered sufficient evidence of the load's performance to proceed to final assembly and commencement of hot testing of the experiment.

2.7 References

1. Konoplev I. V., et al., 2006, *APL*, **89**(17), article: 171503.

3. Experimental Testing of the X-band SIBWO Prototype

Experimental testing of the SIBWO prototype was performed in two stages, initial characterization of the accelerating diode to determine the beam current, followed by characterization of the interaction region.

3.1 Measurement of Transmitted Beam Current

Proper operation of the SIBWO depends on the quality of the electron beam provided by the accelerating diode. Given the self-insulating nature of the diode (in line with that of the source as a whole) the key control parameters were the A-K gap spacing and the quasi-electrostatic focusing offered by the electrode geometries. The former could be adjusted throughout the duration of a given experimental run, without breaking vacuum, through adjustment of the linear stage. To facilitate the latter the diode electrodes were designed to be readily removed and replaced with alternatives, though this did require cycling of the vacuum system.

(a)

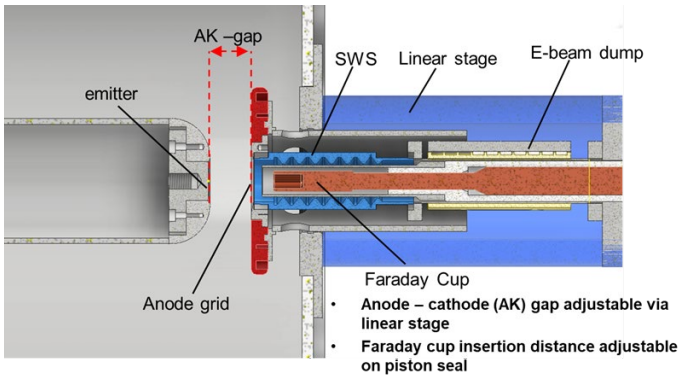

(b)

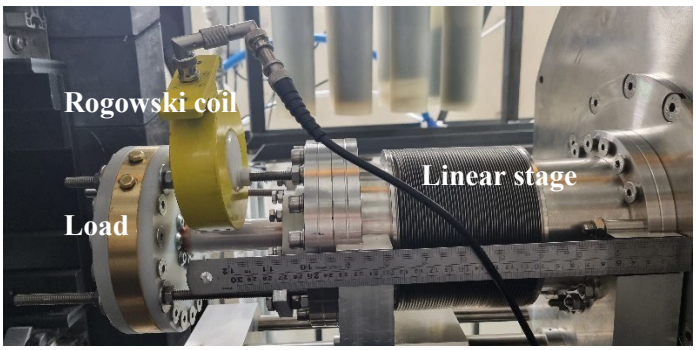

Figure 3.1. Shows (a) the construction of the Faraday-cup diagnostic, fitted within the SIBWO assembly (b) The physical assembly under vacuum, with a load termination and Rogowski coil diagnostic fitted on the ground return.

To measure the current transmitted into the interaction region, while allowing for subsequent testing of the interaction region without alteration to the A-K gap, a Faraday cup was designed that could be inserted into, and removed from, the SIBWO assembly as shown in Figure 3.1. This required a design that allowed for insertion within the SWS, creating a coaxial interaction region with the

Faraday cup stalk forming the inner conductor. To mitigate against the potential generation of RF in this region an intermediate metallic "shield" was placed between the SWS and the Faraday cup. This was electrically connected to the main SIBWO output waveguide in the region of the beam dump, shorting any current collected by the shield to ground, while the current collected by the cup was taken out to a high-power, low impedance, load termination (Figure 3.1(b)). A $0.1 V/A$ Rogowski coil was placed on the ground return from the load to monitor the collected current.

The Faraday cup design was expected to collect only a portion of the current transmitted into the interaction region. To quantify this a model was constructed in CST Particle Studio, providing the predicted performance curves given in Figure 3.2 for an A-K gap of $25 mm$ (the numerically optimized gap spacing).

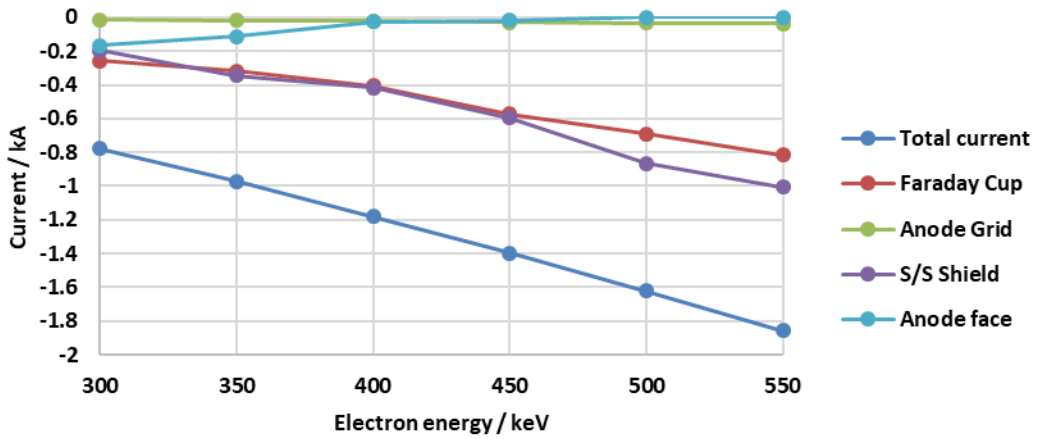

Figure 3.2. Predicted performance of the Faraday cup diagnostic using CST Particle Studio for an A-K gap spacing of 25mm.

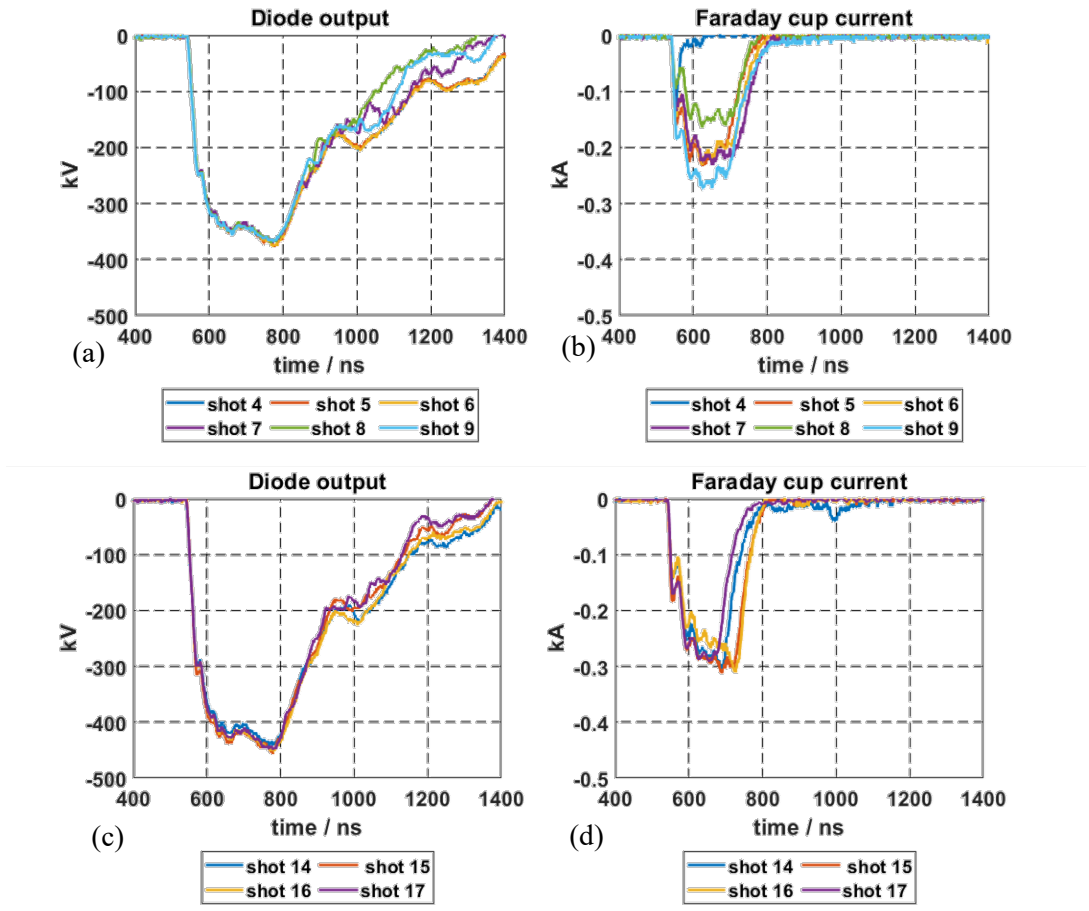

Figure 3.3. Shows (a) – (b) applied potential pulses at ~ 360kV and corresponding collected current traces, (c) – (d) applied potential pulses at ~420kV with corresponding collected current traces.

Results from testing of the accelerating diode, configured to match the design shown in Figure 1.2 with the A-K gap set at $25mm$, are given in Figure 3.3 for PPS output pulses at $\sim 360kV$ and $\sim 420kV$. Reasonable agreement between the predicted and collected current was obtained at $\sim 360kV$, however increasing the applied potential resulted in curtailment on the collected current at a limit of $\sim 300A$, with the pulse duration reducing as the potential was further increased. The most likely route cause of this was "shorting" within the diagnostic due to the proximity of the different metallic components. This could be mitigated through a redesign of the Faraday cup as a stand-alone diagnostic; where the Faraday cup is inserted in place of the interaction region, necessitating disassembly and reassembly of the system as one moves from beam measurement to characterization of the interaction region. However, the reproducibility of results observed at lower voltage provided an alternative means of characterizing performance.

As established in Section 1.4.1, the current emitted for a given applied potential is governed by the geometric parameter known as the Perveance. With the collected current established at $\sim 360kV$

as being $\sim 250A$, mapping to a total emitted current of $\sim 1kA$ (Figure 3.2), equation (1) then provides an estimate of the emitted current, at $\sim 500kV$ as being $\sim 1.6kA$. This was sufficient to move to hot testing of the SIBWO interaction region with slight adjustment of the A-K gap undertaken to vary the transmitted current as required.

Following removal of the Faraday cup a borescope camera was used to check the internal surfaces of the prototype.

Figure 3.4. Shows the grid and emitter surfaces following characterization of the accelerating diode, photographed in-situ with the SIBWO interaction region attached.

Some evidence of heating was observed in the focus electrode but no clear damage was seen on either the emitter surface or anode grid.

3.2 First Operation of the X-band SIBWO Prototype

A series of experiments on the SIBWO prototype were undertaken with alterations to the accelerating diode geometry made between each run. The results obtained are provided in the following sub-sections. In each case the microwave diagnostic lines incorporated a band-pass filter that effectively removed any content below the WG16 cut-off frequency of $\sim 6.5GHz$ and heavily attenuated any signals above $\sim 12GHz$. Microwave measurements were taken on a TEKTRONIX TDS6124C $12GHz$ Deep Storage Oscilloscope (DSO) capable of $40Gs/s$ on two-channels or $20Gs/s$ over four channels. The output from the PPS and the power envelopes of the SIBWO were recorded using a Keysight $200MHz$ DSOX2024A.

3.2.1 Initial Accelerating Diode Geometry

Directly following the beam current measurements presented in Section 3.1 the Faraday cup was removed with the experiment progressing to hot testing of the interaction region itself. A series of shots were taken, providing the output pulse shown in Figure 3.5.

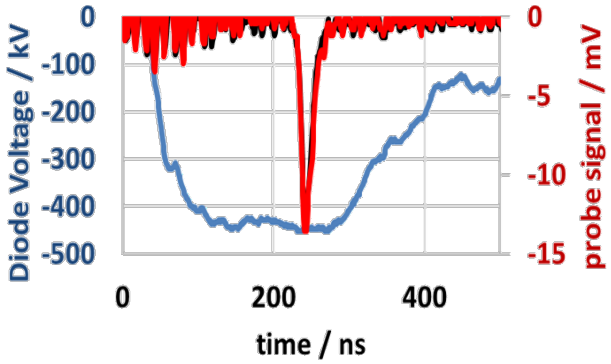

Figure 3.5. First microwave output from the SIWBO.

The output shown in Figure 3.5 was obtained at an applied diode potential of $\sim 440kV$. The microwave signal was measured on probes 1 and 3 from probe-set 1 (orthogonal probes aligned with the x and y axis respectively). Each diagnostic line terminated in a rectifying diode, with the output power envelopes taken to the DSO. Direct AC measurement was not taken in the initial experiment, however the use of the band-pass filter gave confidence the resonant frequency lay within the X-band; for the accelerating potential Figure 1.7 indicated the resonant frequency should be $\sim 9.3GHz$.

The FWHM pulse duration was $\sim 50ns$ with subsequent shots showing rapid degradation in performance. On examination of the experimental assembly significant deposition of metallic material was observed on the emitter surface.

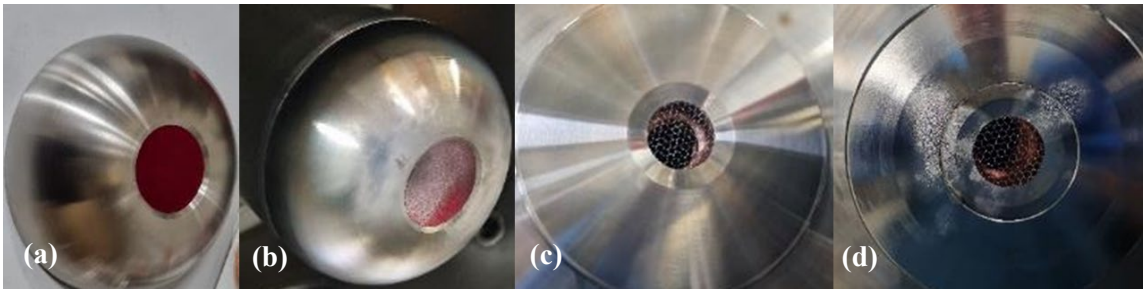

Figure 3.6. Shows (a) the focus electrode and emitter (red) prior to the experimental run (including the diode characterization), (b) same following the initial SIBWO hot test, (c) the anode plate and grid prior to testing, (d) same following initial testing.

While some wear to the emitter velvet was evident there was also notable emission from the focus electrode, resulting in damage to the anode face, followed by deposition of material from the anode

back onto the cathode. The metallization of the emitter rapidly reduced the performance of the diode; in total ten shots close to full voltage ($> 400kV$) were taken, with the diode configured as shown, before the emitter was considered "dead".

3.2.2 Domed Emitter surface

As an initial step in improving the diode performance the flat emitter was replaced with a slightly domed one. This shifted the center of the emitter velvet proud of the focus electrode ($\sim 1mm$ forward of the "flat" position). The intention was to increase the E-field stress on the velvet at that point, preferentially lighting the emitter and reducing the local field-stress on the focus electrode.

To protect the sensitive high-frequency DSO the experimental run again began with measurement of the rectified signals only. Examples of the recorded output are shown in Figure 3.7.

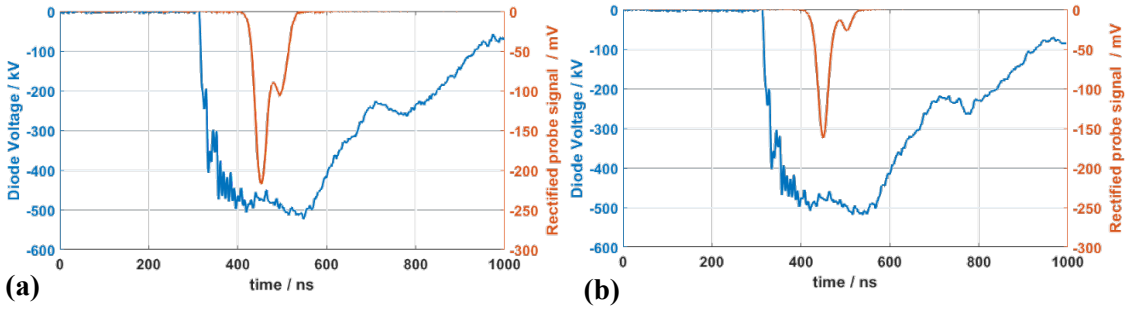

Figure 3.7. Shows (a) first output from the SIBWO at ~ 500kV, (b) Output recorded in subsequent shot.

The power envelopes shown in Figure 3.7 represent the raw data recorded on the DSO with an additional $20dB$ attenuation in each line. The signal magnitude in Figure 3.7(a) therefore correspond to an output power approximately an order of magnitude higher than in the previous experiment and showing a FWHM pulse duration of $\sim 100ns$. Subsequent shots showed degrading performance, again indicating rapid aging in the diode.

The high-frequency DSO was then connected to the experiment, with the AC output from Probe 1 fed through an HP 873XX $10dB$ directional coupler, with the $10dB$ arm used to record the AC signal and the through arm terminated in the rectifying diode. The recorded AC waveform is shown in Figure 3.8 along with its spectral content.

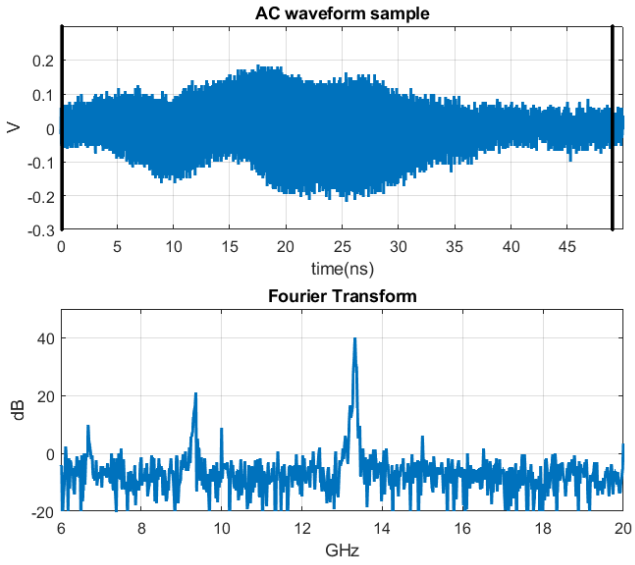

Figure 3.8. Shows the first recorded AC waveform from the SIBWO, along with the spectral content.

The diode emitter failed following the shot shown in Figure 3.8. By this stage in the run the performance had dropped significantly, though Fourier analysis of the output indicted resonance at the correct frequency of $\sim 9.4GHz$ and also the excitement of a known parasitic oscillation with the TE_{21} at $\sim 13.5GHz$.

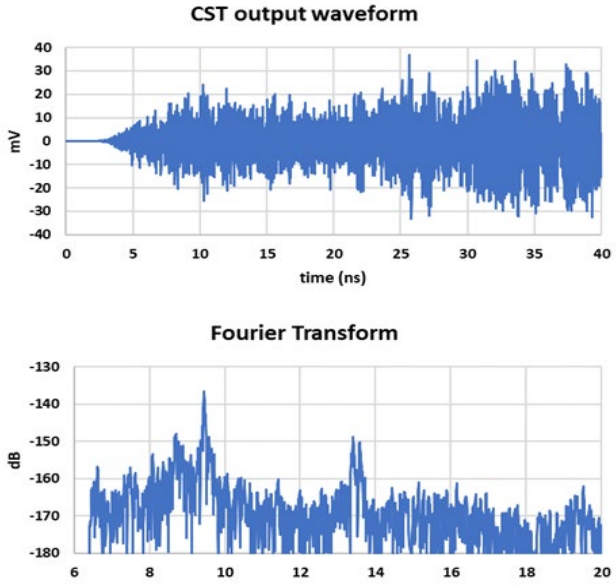

Figure 3.9. Shows the predicted output from the SIBWO with a low-quality electron beam at $500keV, 0.7kA$.

This had been observed in numerical modeling of the SIBWO when the beam quality and beam current were reduced, as shown in Figure 3.9. Examination of the accelerating diode supported such degradation in the beam.

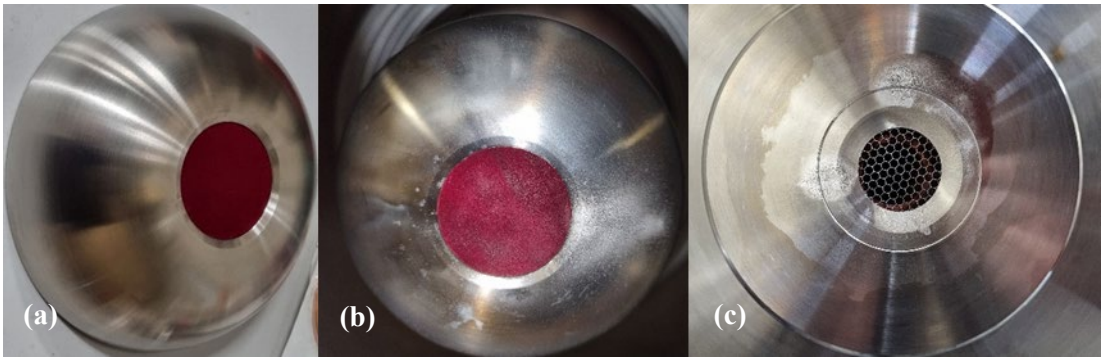

Figure 3.10. Shows the emitter (a) before and (b) after the experimental run, (c) shows the corresponding damage on the anode face.

The extent of metallization on the emitter was reduced when compared to Figure 3.6(b), as was the extent of the damage to the anode face, indicating better transport of the electron beam into the interaction region. Metallization was however still present and more aging of the velvet was apparent, both of which would contribute to the observed rapid degradation in performance.

3.2.3 Polishing of Electrodes

To aid in reducing emission from the focus electrode, and any field enhancement at the anode-face, different methods of polishing the surfaces beyond the finish obtained from the CVC lathe were investigated.

While electropolishing had the expected effect of smoothing micro-structures on the metallic surfaces, producing a notably shinier finish, the extent of damage observed following an experimental run was notably higher.

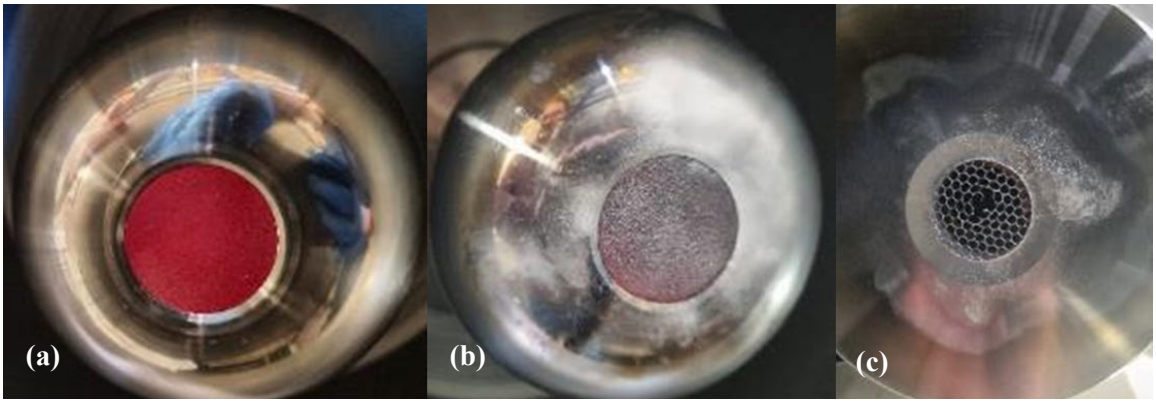

Figure 3.11.shows the cathode (a) before and (b) after ten shots, (c) damage to the anode.

This was attributed to “sharpening” of machining lines left by the CNC tooling on the electrode surfaces; these were readily visible on the focus electrode following the experiment. Methods of improving the finish obtained from the in-house CNC facilities at the UoS are under investigation to enable a higher quality surface finish in future electrode manufacture.

Conventional polishing of the electrode surfaces was more successful at mitigating against spurious emission. Examples of the cathode assembly, before and after testing, along with the anode can be seen in Figure 3.12.

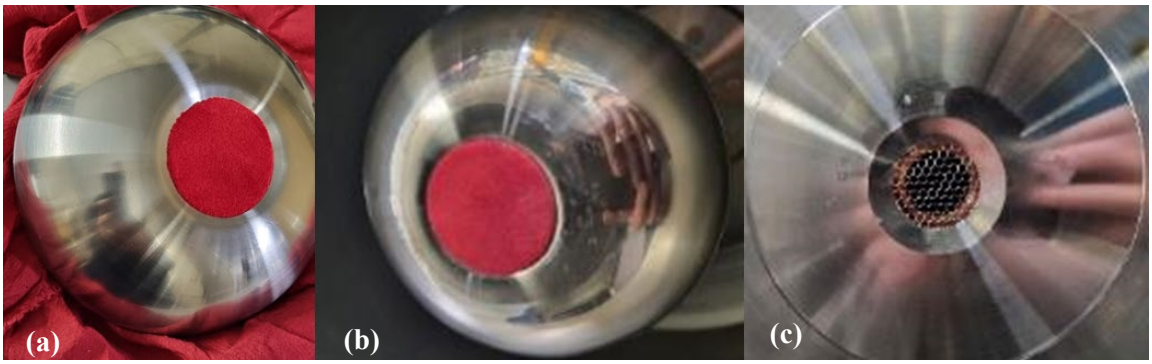

Figure 3.12. Shows the cathode assembly (a) before and (b) after an experimental run, (c) damage to the anode.

As can be seen evidence of damage was markedly reduced, with little sign of emission or material deposition on the focus electrode, minor damage on the anode face and no observable metallization of the emitter velvet.

An unexpected effect of this was evidence of a lack of emission from the cathode velvet. In previous experiments emission from the velvet would be required to pass any meaningful electron beam into the interaction region (the trajectories of emission from the focus electrode all falling on the anode face). It is currently assumed the change in field-stress at the focus electrode, from polishing the surface, negatively impacted on the field-stress on the velvet, dropping it below the threshold required for efficient space-charge-limited emission. Extended testing at the default A-K gap of 25mm showed little evidence of emission and no recorded microwave output.

The diode was reassembled and a further experimental run was undertaken, reducing the A-K gap in $1mm$ steps. This recovered microwave output, though again at the expense of diode life-time. Best output from this experimental run is shown in Figure 3.13, taken at an A-K gap spacing of $15mm$.

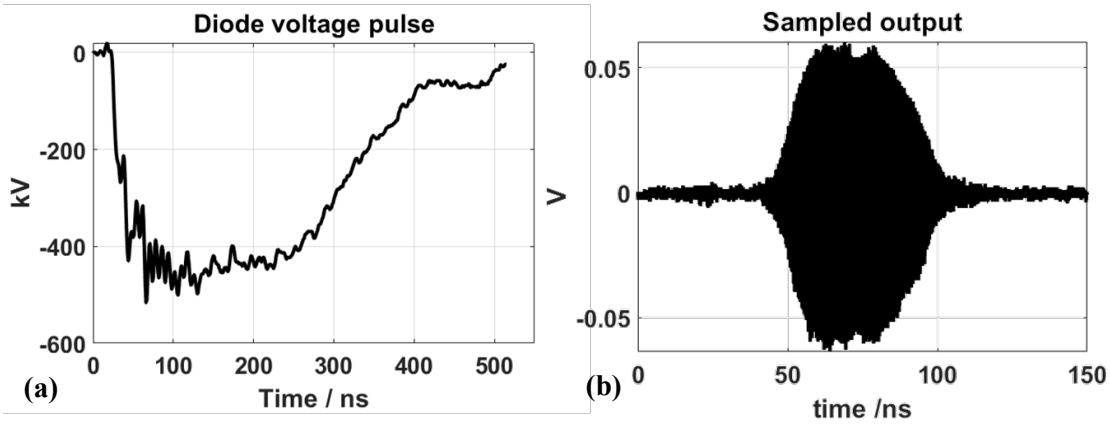

Figure 3.13. Shows (a) the applied diode pulse (b) the measured microwave output from the SIBWO.

The output voltage from the Marx for the pulse shown in Figure 3.13(a) was $\sim 750kV$, with the expected applied potential on the diode being $\sim 500kV$ from an effective PPS load impedance of $\sim 15\Omega$. The reduced output to $\sim 420kV$ indicated the impedance was closer to being matched ($\sim 5\Omega$), which in turn indicated higher than intended currents flowing in the diode. The following shots showed no output, with the diode then opened to investigate. Damage to both the cathode assembly (deposition and emission) was in-line with that observed previously, however the damage to the anode was more severe.

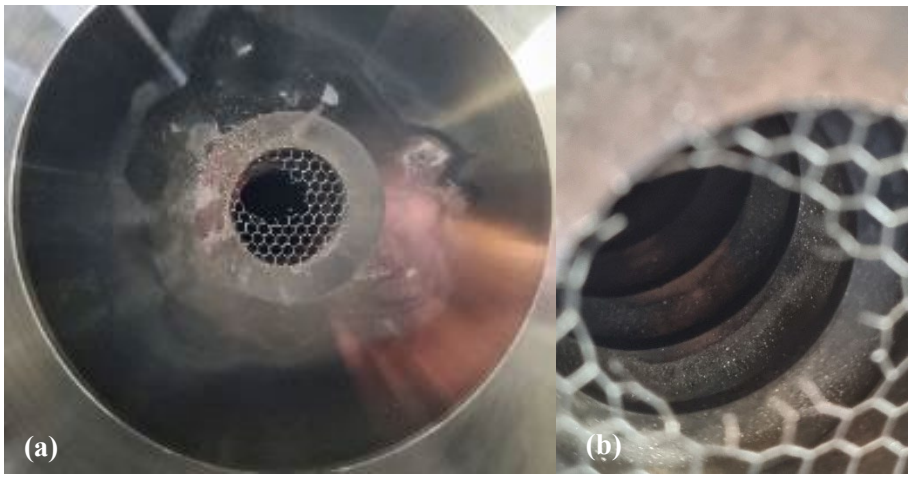

Figure 3.14. Shows (a) damage to the anode grid (b) deposition of material along the SWS.

This was in-line with the damage one would expect to see for a beam current $> 10kA$ impacting on the anode-face. Determination of the transmitted portion was not possible at the time of the experiment; some estimations may however be made from comparison with numerical predictions.

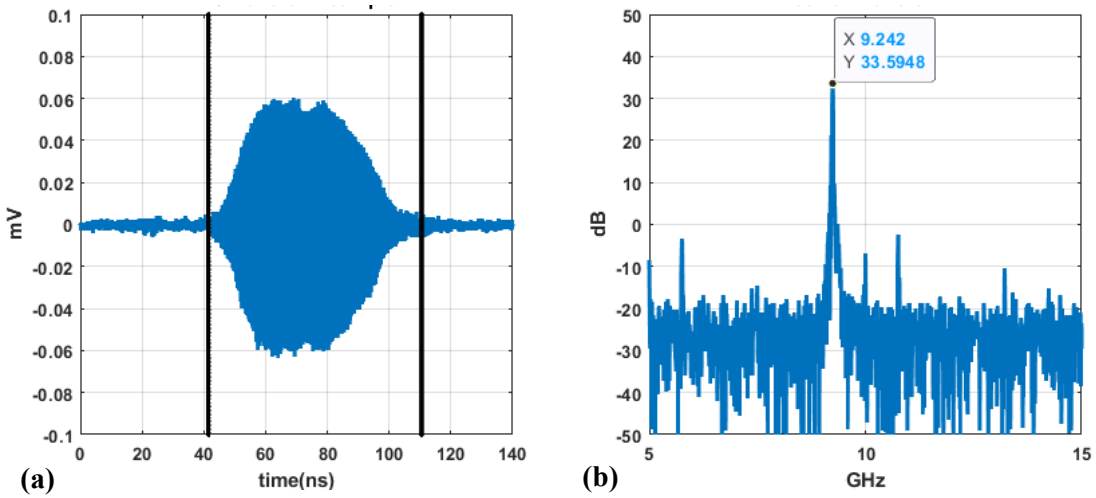

Figure 3.15. Shows (a) windowing of the AC waveform, (b) spectral content in the pulse.

Figure 3.15(b) shows the spectral content of the measured output pulse, obtained when driving the SIBWO at $\sim 420keV$. From Figure 1.7, the predicted output frequency from a $420keV \sim 1.5kA$ beam (scaled from $500keV, 2kA$ using equation (1)) was $\sim 9.3GHz$. Both the beam fill-factor (the ratio of the beam's cross-section to that of the drift-tube) and the beam current impact on the resonant frequency, with increasing beam current and decreasing fill-factor both reducing the resonance. From this it can be surmised that the transmitted beam current was likely in excess of $1.5kA$ and that the beam cross-section did not fill that of the interaction region. Further, the purity of the spectral content indicates the maximum current was probably less than $3-5kA$, as numerical modeling predicts that excitement of parasitic oscillations should be clearly evident at that level.

The spectral purity also indicates that the bulk density of the transmitted beam was well aligned with the central axis, as opposed to off-center as may be surmised by the location of the hole in the grid. Off-axis propagation, or any other notable asymmetry in the cross-section of the beam as it propagates, would cause a notable increase in the excitement of the azimuthally asymmetric mode resonances which was not observed.

The total attenuation in-line between the SIBWO output signal and DSO (including the contribution from the probe) was $\sim 114dB$. Accounting for this gave an estimated output power of $\sim 8MW$, as shown in Figure 3.16.

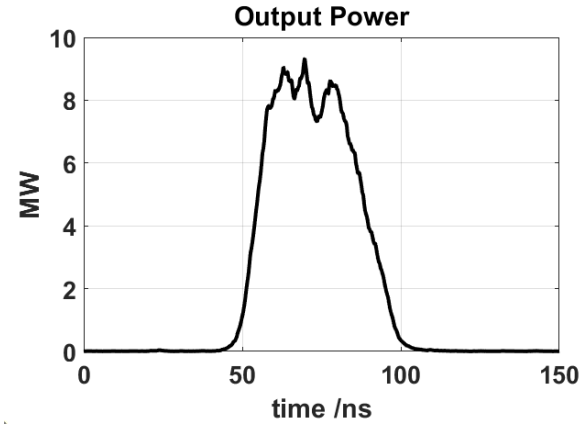

Figure 3.16. Shows the calculated power envelope obtained from the AC output from the SIBWO, accounting for the cold-measured attenuation.

Working from initial estimates of the potential transmitted beam current this would give a best case efficiency of $\eta \sim 1\%$. Repeated cold-calibration of the measurement circuit confirms the attenuation as being $\sim 114dB$, however there are clear aspects to the pulse that dispute the low efficiency.

A relatively high transmitted current would tally with the relative timing seen between the applied potential reaching its peak and the rise-time of the microwave output (see Figure 3.13). This indicates the start current for the oscillation had been exceeded prior to the peak of the applied potential. Such a situation can result in rapid growth, then loss of coherence, however this is typically accompanied by clear evidence of competing oscillations in the spectral content (it is this competition that leads to the loss of coherence) that was not present in the experiment.

In the numerical investigation, while outputs showing coherent behavior were observed at comparable output powers, these were all cases where the beam current was "low" for a given bulk beam energy and / or the applied potential pulse began to "fall" soon after the onset of oscillations. A general example this behavior is shown in Figure 3.17, where the duration of the e-beam injected into the SIBWO numerical model was varied over $30 - 100ns$, with all other control parameters unchanged ($500keV \pm 5\%, 1kA$, 1% angular spread, 90% cross-sectional "fill-factor).

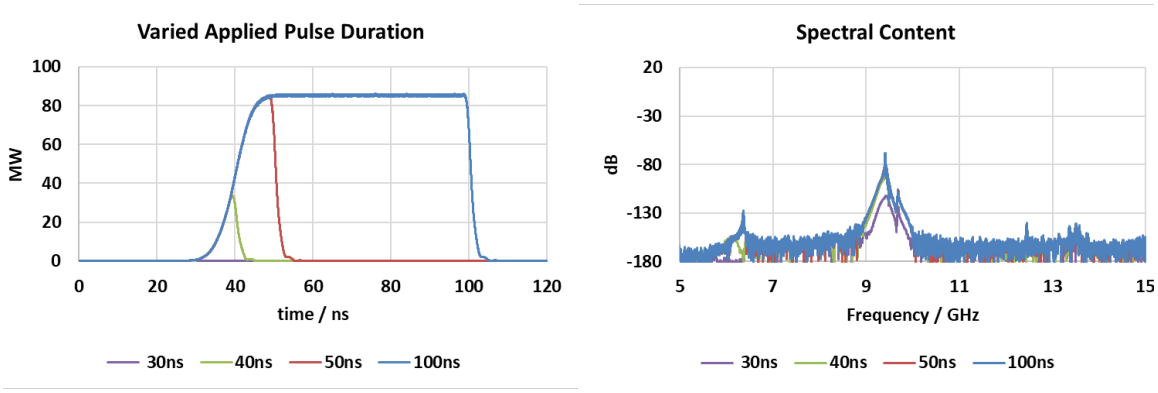

Figure 3.17. Shows the change in the output power envelope, and associated spectral content, for a fixed set of e-beam parameters with varying beam-pulse duration.

Looking at Figure 3.17, for electron beam durations greater than $40ns$ the spectral content associated with the output microwave pulses was largely unchanged, while the power envelopes, taken in isolation, look markedly different. The control of the rise and fall time of the electron beam is limited in the numerical model, however the general pulse-shapes seen for the $40ns$ and $50ns$ cases have clear similarities with the experimentally measured power envelope in Figure 3.16.

Curtailment of the electron beam in the experiment would most likely occur due to "shorting" of the accelerating diode, which would be evident in a collapse of the diode potential, which was not observed in the experiment (see Figure 3.13). An alternative solution, that would produce a microwave pulse with the spectral purity and pulse magnitude observed would be shorting of the field probes. This would occur when the field-stress on the probe tips induced the creation of localized plasma, shorting the tips to the drift-tube body and / or effectively screening them from the rest of the microwave pulse.

Experimental verification of this supposition requires the design and implementation of a secondary diagnostic, which falls outside the time-frame of the current work program. It does however bring this result into line with the very good agreement otherwise seen between the experimental and numerical investigations and is considered a key component for investigation in any future work.

4. Findings and Conclusions

Examination of the SIBWO concept at X-band has shown potential for the development of an efficient, practical HPM source, with significantly lower overall energy and footprint requirements when compared to conventional HPM sources.

The predicted electronic efficiency from the SIBWO, as currently developed, was in the range $20-30\%$, depending on the applied potential and resulting electron beam parameters. The predicted efficiency for the design progressed to experiment was 25%, corresponding to $\sim 220MW$ at $\sim 9.4GHz$ extracted from a high-quality $500keV, \sim 1.8kA$ electron beam.

In experiment two outstanding issues were identified.

1) Degradation of performance in the accelerating diode
2) Lower than predicted output power

In regards to (1), emission from the focus electrode and the subsequent damage observed on the anode and emitter surfaces was largely mitigated through appropriate processing of the electrode surfaces. Further iteration of the diode design, coupled with consideration of different materials (e.g. tungsten for the electrodes, carbon nanotube arrays for the emitter), would address the remaining issues surrounding the aging of the emitter velvet.

In regards to (2), the current estimate for the experimental SIBWO output power is an order of magnitude lower than predicted in simulation. This is, at least in part, associated with the issue identified in the accelerating diode. An in-depth analysis of the experimental results, against the predicted trends in performance, indicates there may also be an issue with the output diagnostic when placed under sufficient electrical stress. As this could not be confirmed within the time-frame of the current program the UoS would consider the stated output power of $\sim 8MW$ at $\sim 9.25GHz$ as being representative of the minimum power generated in experiment.

5. Potential Future Work

The UoS considers the following to be areas of interest in further developing the SIBWO.

- Optimization of the electron accelerating diode
  - Operation of the SIBWO is reliant on the delivery of a suitably high-quality electron beam
  - Resolve remaining issue with aging of emitter material
    - Investigate use of different materials for electrodes and emitter
  - Knowledge gained directly applicable to the accelerating diodes of a range of HPM sources
- Investigate operation of field diagnostic at high-power
  - Test using high-power signals from other sources
  - Develop secondary diagnostic for cross-checking in SIBWO hot tests
- Numerical investigation of X-band SIBWO at lower accelerating potentials
  - Reduced E-field stress in accelerating diode
  - Determine potential output powers and efficiencies for $200-300keV$ electron beams

6. Collaborations

Collaboration with Dr. Simon Cooke and Dr. Igor Chernyavskiy at NRL in modeling and design of the electron accelerator.

7. Personnel

Principal investigator: Prof. Dr. Alan D. R. Phelps
Person months worked: 16
National Academy Member: yes
Nationality: UK

Co-investigator or Co-PI: Prof. Dr. Kevin Ronald
Person months worked: 16
National Academy Member: Yes
Nationality: UK

Team Members: Dr. Philip MacInnes
Person months worked: 48
National Academy Member: No
Nationality: UK

Business Contact: Research & Knowledge Exchange Services (RKES), University of Strathclyde

8. Students

One undergraduate Masters (M.S.) student undertook a final year research project with direct relevance to the current work program; investigating the feasibility of operating a SIBWO at lower electron energy.

9. Technology Transfer

We have undertaken collaborative discussions with Dr. Simon Cooke, NRL, regarding the configuration and simulation of the electron accelerator and interaction region.

10. Products, Publications, Patents, License Agreements, etc.

Publications resulting from this project:

Conference Papers

(1) Enhanced Operation from a Self-Insulating X-Band Backward Wave Oscillator, P. MacInnes, S. J. Cooke, I. A. Chernyavskiy, K. Ronald, A. D. R. Phelps, *2019 UK-US Directed Energy Workshop*, Shrivenham, UK, 22 – 26 July 2019.
(2) Self-insulation of a high-power Cherenkov oscillator, operating in the X-band, P. MacInnes, S. J. Cooke, I. A. Chernyavskiy, K. Ronald, A. D. R. Phelps, *47th IEEE International Conference on Plasma Science (ICOPS-2020)*, Virtual Conference, 6-10 December 2020.
(3) Dynamics of highly energetic electrons in novel accelerating diodes, B. Crampsey, P. MacInnes, K. Ronald, A. D. R. Phelps, *47th IEEE International Conference on Plasma Science (ICOPS-2020)*, Virtual Conference, 6-10 December 2020.
(4) A self-confined high-power Cherenkov oscillator operating at high-frequency, P. MacInnes, S. J. Cooke, I. A. Chernyavskiy, K. Ronald, A. D. R. Phelps, *47th UK Institute of Physics, Plasma Physics Conference*, Virtual Conference, 6 – 9 April 2021.
(5) First Experimental Operation of an X-Band Self-Insulating Backward-Wave Oscillator, P. MacInnes, K. Ronald, C. G. Whyte, B. Crampsey, S. J. Cooke, I. A. Chernyavskiy, A. D. R. Phelps, *2022 UK-US Directed Energy Workshop*, Shrivenham, UK, 18 – 22 July 2022.

11. Point of Contact in Navy

Ryan Hoffman ONR, ryan.hoffman@navy.mil
Tim Andreadis NRL, tim.andreadis@nrl.navy.mil
Jesus GilGil NRL, jesus.gilgil@nrl.navy.mil
Simon Cooke NRL, simon.cooke@nrl.navy.mil
Igor Chernyavskiy NRL, igor.chernyavskiy@nrl.navy.mil
Matthew McQuage NSWC, matthew.mcquage@navy.mil
Predrag Milojkovic ONRG (before 2021) , predrag.milojkovic.civ@mail.mil
Charles Eddy ONRG (since 2021), chip.eddy@nrl.navy.mil

REPORT DOCUMENTATION PAGE

Form Approved
OMB No. 0704-0188

1. REPORT DATE *(DD-MM-YYYY)*	2. REPORT TYPE	3. DATES COVERED *(From - To)*
30-09-2022	FINAL	15 June 2018 - 14 June 2022

4. TITLE AND SUBTITLE
Compact high-power microwave oscillators

5a. CONTRACT NUMBER

5b. GRANT NUMBER
NICOP N62909-18-1-2122

5c. PROGRAM ELEMENT NUMBER

6. AUTHOR(S)
MacInnes, Philip
Ronald, Kevin
Phelps, Alan D. R.

5d. PROJECT NUMBER

5e. TASK NUMBER

5f. WORK UNIT NUMBER

7. PERFORMING ORGANIZATION NAME(S) AND ADDRESS(ES)
University of Strathclyde
16 Richmond Street
Glasgow G1 1XT
United Kingdom

8. PERFORMING ORGANIZATION REPORT NUMBER

9. SPONSORING/MONITORING AGENCY NAME(S) AND ADDRESS(ES)
Office of Naval Research Global
86 Blenheim Crescent
Ruislip MX HA4 7HB
United Kingdom

10. SPONSOR/MONITOR'S ACRONYM(S)
ONR/ONRG

11. SPONSORING/MONITORING AGENCY REPORT NUMBER

12. DISTRIBUTION AVAILABILITY STATEMENT
Approved for Public Release;Distribution is Unlimited

13. SUPPLEMENTARY NOTES

14. ABSTRACT Numerical modeling and experimental measurements are reported of a novel high-power X-band ($8-12GHz$) microwave oscillator operating without the application of external magnetic insulation. Radiation is produced by modulation of an electron beam, propagated solely under the beam's self-forces. Numerical modeling indicates efficiencies of $\eta\sim25\%$, corresponding to $\sim220MW$ from a $500keV$, $1.7kA$ electron beam, with efficiencies of $\eta\sim30\%$ obtained as the quality of the electron beam improves through revision of the electron accelerator, informed by the experimental results. Named the 'Self-Insulating Backward-Wave Oscillator' (SIBWO), the prototype design has been manufactured for proof of principle experiments. The electron beam and the microwave output have been measured. The measured output mode TM_{01} and frequency of 9.25*GHz* both agree with the numerical model. The full-width-half-maximum microwave pulse duration ~50*ns* was shorter and the microwave power ~8*MW* was less than in the numerical simulations. Analysis of these results has identified modifications to enable increased output power in future work.

15. SUBJECT TERMS
High power microwaves, vacuum electronics, BWO, SIBWO, compact microwave source, X-band source

16. SECURITY CLASSIFICATION OF:			17. LIMITATION OF ABSTRACT	18. NUMBER OF PAGES	19a. NAME OF RESPONSIBLE PERSON
a. REPORT	b. ABSTRACT	c. THIS PAGE	UU	42	Dr. Charles R. Eddy
U	U	U			19b. TELEPONE NUMBER (*Include area code*) US Mobile: +1 (360) 516-0645